

This work was written as part of one of the author's official duties as an Employee of the United States Government and is therefore a work of the United States Government. In accordance with 17 U.S.C. 105, no copyright protection is available for such works under U.S. Law.

Public Domain Mark 1.0

<https://creativecommons.org/publicdomain/mark/1.0/>

Access to this work was provided by the University of Maryland, Baltimore County (UMBC) ScholarWorks@UMBC digital repository on the Maryland Shared Open Access (MD-SOAR) platform.

**Please provide feedback**

Please support the ScholarWorks@UMBC repository by emailing [scholarworks-group@umbc.edu](mailto:scholarworks-group@umbc.edu) and telling us what having access to this work means to you and why it's important to you. Thank you.

# Bimodal size distribution influences on the variation of Angstrom derivatives in spectral and optical depth space

N. T. O'Neill<sup>1</sup>, T. F. Eck, B. N. Holben, A. Smirnov and O. Dubovik

NASA Goddard Space Flight Center, Greenbelt, Maryland

A. Royer

CARTEL, Université de Sherbrooke, Sherbrooke, Québec, Canada

**Abstract.** The variation of the aerosol optical depth and its first and second spectral derivatives ( $\alpha$  and  $\alpha'$ ) can be largely described in terms of the spectral interaction between the individual optical components of a bimodal size distribution. Simple analytical expressions involving the separate optical components of each mode explain virtually all the features seen in spectra of the aerosol optical depth and its derivatives. Illustrations are given for a variety of measured optical depth spectra; these include comparative simulations of the diurnal behavior of  $\alpha$  and  $\alpha'$  spectra as well as the diurnal and general statistical behavior of  $\alpha$  and  $\alpha'$  as a function of optical depth (optical depth space). Each mode acts as a fixed "basis vector" from which much of the behavior in spectral and optical depth space can be generated by varying the extensive (number density dependent) contributions of fine and coarse mode optical depths. Departures from these basis vectors are caused by changes in aerosol type (average size and refractive index) and thus are associated with differing synoptical air masses, source trajectories or humidity conditions. Spectral parameters are very sensitive to interband errors in measured optical depth data. Third-order polynomial fits within the visible-NIR spectral region effectively filter such errors while representing the limit of useful extractable information.

## 1. Introduction

Angstrom [1929] showed that the spectral relation between the logarithm of aerosol optical depth and the logarithm of wavelength is approximately linear. The slope of this relationship across the visible spectral region has become a robust parameter which is indicative of average aerosol dimensions in the submicrometer to supermicrometer particle size range. Departures from linearity in the slope of the logarithm of optical depth versus the logarithm of wavelength are expected [King *et al.*, 1976; Kaufman, 1993] and indeed yield information about the non-Junge types of aerosols which compose real size distributions [e.g., Foitzik, 1964; Nikitinskaya *et al.*, 1973; Tomasi *et al.*, 1983; Stettler and Hoyningen-Huene, 1993; Villevalde *et al.*, 1994; Eck *et al.*, 1999].

Aerosol optics in the ultraviolet to near-infrared portions of the electromagnetic spectrum are largely influenced by a fine (accumulation) mode in the submicron radius range and by a coarse mode in the supermicron radius range. Rather than assuming a more flexible but necessarily more cumbersome optical description in terms of independent discrete bins of a generalized aerosol size distribution, one can take the point of view that most optical phenomena can be adequately described

by an appropriate choice of two or at most three size distribution modes.

The modal spectral interpretation which results is analogous to the Junge/Angstrom approach inasmuch as low-order spectral coefficients lead to a description of nature in terms of optical parameters which are arguably more robust and repeatable than multibin particle size distribution inversions of optical data and which may adequately serve the needs of many users of aerosol optical data. Much like the classical Angstrom coefficient, these indices are not an exact description of nature; rather they are to be viewed in the sense of "equivalent" optical parameters which provide an intuitive framework for the approximate interpretation of microphysical properties. If greater levels of sophistication are needed, then one has the option of proceeding to higher-order spectral moments and/or more detailed modular descriptions of the particle size distribution.

Such simplistic optical parameterizations are often sufficient for the modeling of radiative transfer phenomena and the associated applications such as the atmospheric correction of satellite imagery. The insights offered by the casting of aerosol optical behavior in a more fundamental and robust formulation can yield important benchmarks for the validation of aerosol dynamics in climatological models. The bimodal approach also permits simple and purely optical techniques to be developed where the goal is to extract average and characteristic spectral coefficients for each separate particle size mode from the general spectral behavior of the aerosol optical depth. These modal spectral coefficients can in turn be used to extract microphysical parameters at a commensurate level of sophistication (for example, an effective or mean modal radius

<sup>1</sup>Now at CARTEL, Université de Sherbrooke, Sherbrooke, Québec, Canada.

being derived from the Ångström coefficient associated with that mode [O'Neill and Royer, 1993; Shifrin, 1995].

In this paper we demonstrate that simple analytical expressions derived from a bimodal parameterization of aerosol particle size distributions permit one to explain many of the features seen in the measured spectra of the aerosol optical depth and its first and second spectral derivatives. These expressions capture the essence of what the bimodal approach contributes to the understanding of aerosol optics; that much of the variation observed in spectral optical depth parameters is due to changes in the extensive character of the bimodal components (due to changes in their abundance or integrated vertical number density) rather than changes in the average size or composition of each component. It is our hope that the bimodal approach presented in this paper will permit a more intuitive understanding of optical depth spectra and lead to alternate and standardized techniques for interpreting these spectra.

## 2. Theoretical Background

The total aerosol optical depth can be expressed as a linear sum of the optical depth of the fine (*f*) and coarse (*c*) modes;

$$\tau_a = \tau_f + \tau_c \quad (1a)$$

This relationship can be written explicitly in terms of single particle (average) extinction cross sections which can be viewed as basis vectors for the generation of all optical depths sharing the same intrinsic mode properties (size and refractive index);

$$\tau_a = A_f C_f(\lambda) + A_c C_c(\lambda), \quad (1b)$$

where  $A_f$  and  $A_c$  are the vertically integrated number density (abundance) and  $C_f(\lambda)$  and  $C_c(\lambda)$  are the extinction cross sections of the fine and coarse mode respectively. The Ångström coefficient in its most general form can be written as

$$\alpha = -\frac{d \ln \tau_a}{d \ln \lambda}. \quad (2)$$

Given  $d\tau/d\ln\lambda = \tau d\ln\tau/d\ln\lambda$ , one can perform a linear operation on equation (1) and express the overall Ångström coefficient as the weighted mean [O'Neill and Royer, 1993; Shifrin, 1995]

$$\alpha = \frac{\alpha_f \tau_f + \alpha_c \tau_c}{\tau_a}, \quad (3)$$

where it must be kept in mind that the component Ångström coefficients ( $\alpha_f$  and  $\alpha_c$ ) as well as the component optical depths are in general functions of wavelength. It is worth underscoring as well that  $\alpha_f$  and  $\alpha_c$  (like  $C_f$  and  $C_c$ ) are dependent only on average particle characteristics (size and refractive index). Equation (3) can be expressed more succinctly as a function of only one weighting variable;

$$\alpha = \alpha_f \eta + \alpha_c (1 - \eta), \quad (4)$$

where  $\eta = \tau_f / \tau_a$  (as per the notation of Tanré et al., [1999]). The second order derivative  $-d^2 \ln \tau_a / d \ln \lambda^2$  or equivalently the derivative of the Ångström coefficient ( $\alpha'$ ) can then be applied to (4);

$$\alpha' = \alpha'_f \eta + \alpha'_c [1 - \eta] - \eta [1 - \eta] (\alpha_f - \alpha_c)^2. \quad (5)$$

A plot of  $\alpha$  or  $\alpha'$  versus  $\tau_a$  for a fixed wavelength ("optical depth space") will clearly be intrinsically related to a spectral plot of these same parameters. This type of relationship is worth considering since  $\alpha$  versus  $\tau_a$  graphs are a common and convenient means of representing size and columnar density information in two dimensions [e.g. Smirnov et al., 1994; Ahern et al., 1991]. In optical depth space, one must bear in mind that the component optical depths  $\tau_f$  and  $\tau_c$  are, for fixed modal size distributions and refractive indices, functions of abundance. Inasmuch as they are unique functions of time, they can as well be described as functions of each other and as functions of  $\tau_a$ .

In terms of equations (4) and (5) this translates into  $\alpha$  and  $\alpha'$  being functions of  $\tau_a$  through their dependence on  $\eta$  (explicitly, one replaces  $\eta(\tau_a)$  for  $\eta$  in these two equations). The behavior of  $\alpha$  and  $\alpha'$  in optical depth space can then be described by higher- order derivatives and their zeros. The first-order derivatives are given by simple analytical forms;

$$\left( \frac{\partial \alpha}{\partial \tau_a} \right)_\lambda = (\alpha_f - \alpha_c) \left( \frac{\partial \eta}{\partial \tau_a} \right)_\lambda, \quad (6)$$

$$\left( \frac{\partial \alpha'}{\partial \tau_a} \right)_\lambda = \{ (\alpha_f - \alpha_c)^2 [2\eta - 1] + (\alpha'_f - \alpha'_c) \} \left( \frac{\partial \eta}{\partial \tau_a} \right)_\lambda \quad (7)$$

where the derivative of the optical ratio  $\eta$  is given by;

$$\left( \frac{\partial \eta}{\partial \tau_a} \right)_\lambda = \frac{\xi}{\tau_a^2} \quad \text{where} \quad \xi = \tau_c \left( \frac{\partial \tau_f}{\partial \tau_a} \right)_\lambda - \tau_f \left( \frac{\partial \tau_c}{\partial \tau_a} \right)_\lambda \quad (8)$$

The influence of this latter derivative can relevantly be illustrated by noting that for the case of an influx of fine mode particles  $\tau_c = \text{constant}$ ,  $\xi = \tau_c / \tau_a^2$  and thus that the two derivative expressions of equations (6) and (7) are fundamentally controlled by a  $1 / \tau_a^2$  product term.

In the sections that follow we give illustrations using both simulations and real data to demonstrate how these simple analytical expressions describe much of the behavior of the aerosol optical depth and its derivatives in spectral and optical depth space.

## 3. Illustrations With Simulated Data

### 3.1. Spectral Curvature Parameters in Spectral Space

Table 1 summarizes all the analytical expressions for the optical depth spectral derivatives as well as critical spectral points for a conceptual bimodal Ångström size distribution and a generalized bimodal size distribution. A brief interpretation of these mathematical results in terms of simulated optical depth spectra is presented in this section.

**3.1.1. Bimodal Ångström case.** It is instructive to consider an idealized "Ångström" bimodal size distribution case in order to better appreciate the spectral behavior of more realistic bimodal size distributions. Here one imagines two modes whose spectral behavior is governed by different Ångström power laws. Even in the absence of spectral curvature in the separate modal contributions there is a curvature brought about by the optical depth averaging between the two modes. The left-hand

graphs in Figure 1 show this effect where the spectral optical depth behavior of each mode (the dashed curves) is governed by a linear Ångström-type relation. It can be clearly seen that the total of the two optical depths on a log-log scale (asterisks) is nonlinear and that the Ångström coefficient spectrum is a simple weighted mean between the constant Ångström coefficients of each mode ( $\alpha_f$  and  $\alpha_c$ ). The decrease in  $\alpha$  from the asymptote of  $\alpha_f$  for small wavelength (where  $\tau_f \gg \tau_c$  or  $\eta \rightarrow 1$ ) to the asymptote of  $\alpha_c$  for large wavelengths (where  $\tau_f \ll \tau_c$  or  $\eta \rightarrow 0$ ) means that  $\alpha'$  is always negative with a minimum at the wavelength for which the modal optical depths are equal ( $\eta = 0.5$  at  $\lambda_{inf}$ ).

**3.1.2. General bimodal case.** In reality each mode has its own spectral curvature which supplements the curvature due to modal averaging. The right-hand side of Figure 1 illustrates the case of a typical northeastern U.S. coastal aerosol whose  $\alpha_f$  value increases in an almost linear fashion with  $\ln \lambda$  across the visible-NIR spectrum. Eck *et al.*, [1999] showed this aspect of strong linearity for fine-mode-dominated bio-mass burning aerosols at large aerosol optical depths. The increase becomes distinctly nonlinear, however, as the upper wavelength of the spectral interval increases. The increase in the dashed  $\alpha_f$  curve with increasing wavelength (middle right-hand graph of Figure 1) is symptomatic of more general trends; the Ångström coefficient of the scattering component of the total extinction optical depth

tends toward an asymptotic value of 4 for very small particles (or very large wavelengths), and it is this tendency that dominates at shorter wavelengths. In contrast, the absorption component of the total extinction optical depth tends toward an asymptotic value of unity for very small particles or very large wavelength, and it is this tendency that tends to dominate at larger wavelengths when the rapidly decreasing  $\lambda^{-4}$  scattering contribution is rendered negligible compared to the slowly decreasing  $\lambda^{-1}$  absorption component. The combination of these effects produces a spectral maximum in  $\alpha_f$  (not seen in Figure 1 since it is beyond the upper limit of the wavelength scale). This increase in the dashed  $\alpha_f$  curve, which one observes in Figure 1, effectively translates  $\lambda_{inf}$  to the right relative to the pure Ångström case and induces a maximum in  $\alpha$  when the increase due to  $\alpha_f$  is balanced by the decrease due to optical depth averaging between the modes.

### 3.2. Spectral Curvature Parameters in Optical Depth Space

Table 2 summarizes all relevant derivatives and critical points of  $\alpha$  and  $\alpha'$  for both the bimodal Ångström case and the general bimodal case as a function of aerosol optical depth. In this section we give a brief interpretation of these results in terms of simulations in optical depth space.

**Table 1.** Analytical Expressions and Ordinal Points in Spectral Space

| Bimodal Ångström  | Bimodal General   |
|---|---|
| $\tau_a = \tau_f + \tau_c$  | $\tau_a = \tau_f + \tau_c$  |
| $\tau_f = \tau_{f0} \left( \frac{\lambda_0}{\lambda} \right)^{\alpha_f}$ , $\tau_c = \tau_{c0} \left( \frac{\lambda_0}{\lambda} \right)^{\alpha_c}$ | $\tau_f = A_f C_f(\lambda) = \frac{\tau_{f0}}{C_f(\lambda_0)} C_f(\lambda)$ ,<br>$\tau_c = A_c C_c(\lambda) = \frac{\tau_{c0}}{C_c(\lambda_0)} C_c(\lambda)$                |
| $\alpha(\lambda) = \alpha_f \eta(\lambda) + \alpha_c [1 - \eta(\lambda)]$   | $\alpha(\lambda) = \alpha_f(\lambda) \eta(\lambda) + \alpha_c(\lambda) [1 - \eta(\lambda)]$   |
| $\alpha' = -\eta [1 - \eta] (\alpha_f - \alpha_c)^2$  | $\alpha' = \alpha'_f \eta + \alpha'_c [1 - \eta] - \eta [1 - \eta] (\alpha_f - \alpha_c)^2$   |
| $\alpha'' = \eta [1 - \eta] (\alpha_f - \alpha_c)^3 [1 - 2\eta]$  | $\alpha'' = \alpha''_f \eta + \alpha''_c [1 - \eta] - 3\eta [1 - \eta] (\alpha_f - \alpha_c) (\alpha'_f - \alpha'_c) + \eta [1 - \eta] (\alpha_f - \alpha_c)^3 [1 - 2\eta]$ |
| <b>Extrema and Inflection Points</b>  |   |
| Peak or minimum in $\alpha$<br>$\lambda = \lambda_p$ ( $\alpha' = 0$ )<br>when $\eta = 0$ or $1$ or $\tau_f = 0$ or $\tau_f = \tau_a$               | $\lambda = \lambda_p$ ( $\alpha' = 0$ )<br>when $\eta = \eta_{min} \pm \frac{\sqrt{-\alpha'_{min}}}{\alpha_f - \alpha_c}$   |
| Inflection in $\alpha$<br>at $\lambda = \lambda_{inf}$ ( $\alpha'' = 0$ )<br>when $\eta = \frac{1}{2}$ or $\tau_f = \tau_c$                         | at $\lambda = \lambda_{inf}$ ( $\alpha'' = 0$ )<br>when $\eta = \eta_{inf} \leq \frac{1}{2}$ or $\tau_f \leq \tau_c$  |

All spectral derivatives are partial derivatives with vertical number densities held constant.

$$\eta(\lambda) = \frac{\tau_f(\lambda)}{\tau_a(\lambda)}, \quad \alpha_i = -\frac{d \ln \tau_i}{d \ln \lambda}, \quad \alpha'_i = \frac{d \alpha_i}{d \ln \lambda}, \quad \alpha''_i = -\frac{d^2 \ln \tau_i}{d^2 \ln \lambda^2}.$$

$$\frac{d \eta}{d \ln \lambda} = -\eta [1 - \eta] (\alpha_f - \alpha_c)$$

$\eta_{min}$  and  $\alpha'_{min}$  are defined in Table 2.

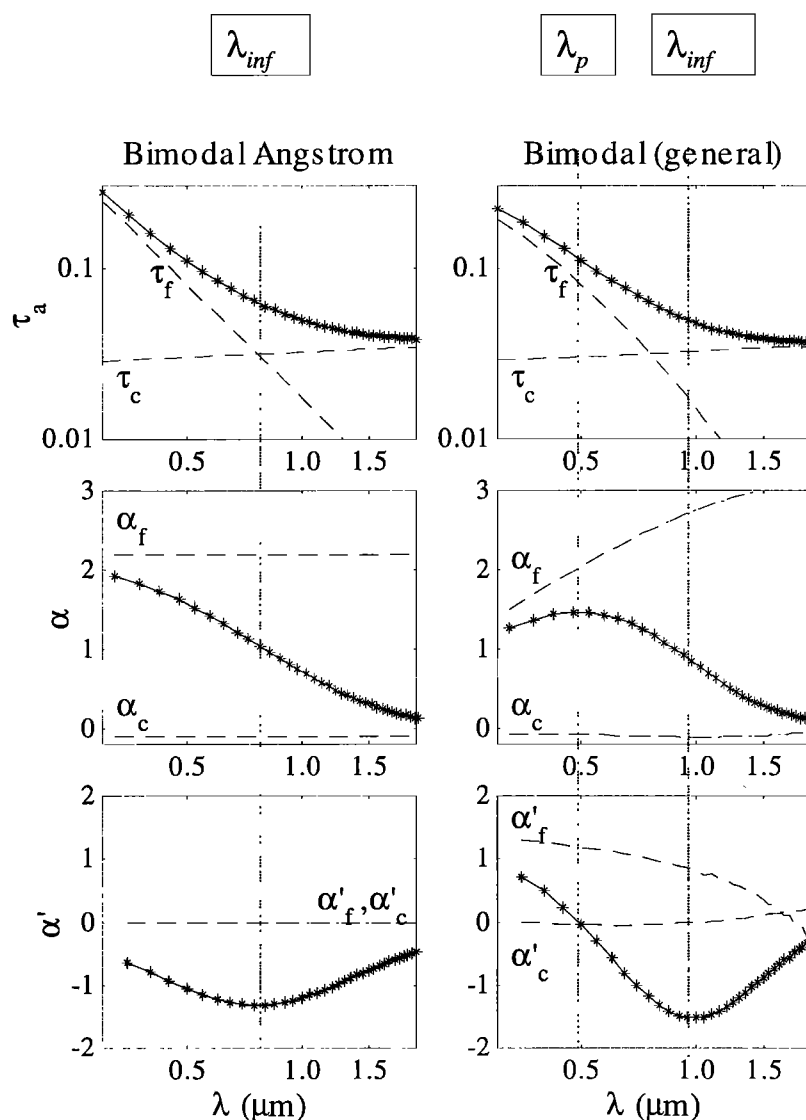


**Figure 1.** Spectra of  $\tau$ ,  $\alpha$ , and  $\alpha'$  (logarithmically scaled wavelength) for the bimodal Ångström case (left-hand set of figures) and the general bimodal case (right-hand set of figures).  $\tau_c$  (500 nm) and  $\tau_f$  (500 nm) were set to 0.08 and 0.03, respectively. Lognormal size distributions [Hansen and Travis, 1974] were used to represent each mode in the general case. The properties of the ACC-1 fine mode and the coarse mode employed in the simulation are given in Table 4. The wavelengths,  $\lambda_p$  and  $\lambda_{inf}$  represent the maximum and inflection points in  $\alpha$  (defined in Table 1).

The graphs of Figure 2 are bimodal Mie simulations which show the effect of a regular increase in the fine mode abundance (represented by a regular increase in  $\tau_f$  (500 nm)) on the  $\alpha$  and  $\alpha'$  spectra of Figure 1. To produce the family of curves observed, the coarse mode optical depth at 500 nm was fixed at 0.03, while  $\tau_f$  (500 nm) was allowed to increase by factors of 2 from 0.01 to 0.64 (the curve of Figure 1 was part of this family and is indicated with asterisks). The three vertical lines shown in this plot represent 500, 650, and 850 nm; the projection in optical depth space of the  $\alpha$  and  $\alpha'$  curves intersecting these lines is shown in Figure 3. By comparing Figures 2 and 3, one can readily appreciate, both in the bimodal Ångström and the general bimodal case, the link between the behavior of the spectral curvature parameters in spectral and optical depth space.

The case of an influx of fine mode particles represented by these figures (corresponding to an increase in  $A_f$  in equation (1b)) is the most dominant type of aerosol event in urban industrial regions or biomass burning regions. This typically means that the coarse fraction is small, while the fine fraction assumes values between  $\tau_f \sim \tau_c$  to  $\tau_f \gg \tau_c$ . For such conditions,  $\alpha'$  increases from a negative value to a positive upper limit of  $\alpha'_f$  (this trend can be readily observed in the bimodal  $\alpha'$  case of Figure 3). The minimum observed in both the Ångström and the bimodal  $\alpha'$  cases of Figure 3 is dependent on the negative "Ångström term" of  $\alpha'$  in Table 1 (the term that varies as the square of  $\alpha_f - \alpha_c$ ). The zero crossing of the increasing trend from negative values near the minimum to positive values at large  $\tau_a$  can be seen in the Figure 3 simulations and is observable in measured data [Eck et al., 1999]. The minimum, which can be

**Table 2.** Analytical Expressions and Ordinal Points in Optical Depth Space

| Bimodal Ångström   | Bimodal General   |
|--|---|
| $\tau_a = \tau_f + \tau_c$   | $\tau_a = \tau_f + \tau_c$  |
| $\alpha(\tau_a) = \alpha_f \eta(\tau_a) + \alpha_c [1 - \eta(\tau_a)]$ $= \alpha_c + (\alpha_f - \alpha_c) \frac{\tau_f}{\tau_a} \text{ or}$ $= \alpha_f - (\alpha_f - \alpha_c) \frac{\tau_c}{\tau_a}$  | $\alpha(\tau_a) = \alpha_f \eta(\tau_a) + \alpha_c [1 - \eta(\tau_a)]$ $= \alpha_c + (\alpha_f - \alpha_c) \frac{\tau_f}{\tau_a} \text{ or}$ $= \alpha_f - (\alpha_f - \alpha_c) \frac{\tau_c}{\tau_a}$ |
| $\left(\frac{\partial \alpha}{\partial \tau_a}\right)_\lambda = (\alpha_f - \alpha_c) \left(\frac{\partial \eta}{\partial \tau_a}\right)_\lambda$  | $\left(\frac{\partial \alpha}{\partial \tau_a}\right)_\lambda = (\alpha_f - \alpha_c) \left(\frac{\partial \eta}{\partial \tau_a}\right)_\lambda$   |
| $\left(\frac{\partial \alpha'}{\partial \tau_a}\right)_\lambda = (\alpha_f - \alpha_c)^2 [2\eta - 1] \left(\frac{\partial \eta}{\partial \tau_a}\right)_\lambda$   | $\left(\frac{\partial \alpha'}{\partial \tau_a}\right)_\lambda = \{(\alpha_f - \alpha_c)^2 [2\eta - 1] + (\alpha'_f - \alpha'_c)\} \left(\frac{\partial \eta}{\partial \tau_a}\right)_\lambda$          |
| <i>Extrema and Inflection Points</i>   |   |
| Minimum in $\alpha'$   |   |
| $\eta = \eta_{\min} \text{ or } \tau_a = \tau_{a, \min} \left(\frac{\partial \alpha'}{\partial \tau_a}\right)_\lambda = 0$   | $\eta = \eta_{\min} \text{ or } \tau_a = \tau_{a, \min} \left(\frac{\partial \alpha'}{\partial \tau_a}\right)_\lambda = 0$  |
| $\eta_{\min} = \frac{1}{2}$  | $\eta_{\min} = \frac{1}{2} \left[ 1 - \frac{\alpha'_f - \alpha'_c}{(\alpha_f - \alpha_c)^2} \right]$  |
| $\alpha'_{\min} = -\frac{(\alpha_f - \alpha_c)^2}{4}$  | $\alpha'_{\min} = \alpha'_c - (\alpha_f - \alpha_c)^2 \eta_{\min}^2$  |
| zero in $\alpha'$  |   |
| see Table 1  | see Table 1   |
| $\left(\frac{\partial \eta}{\partial \tau_a}\right)_\lambda = \frac{\xi}{\tau_a^2} \text{ where } \xi = \tau_c \left(\frac{\partial \tau_f}{\partial \tau_a}\right)_\lambda - \tau_f \left(\frac{\partial \tau_c}{\partial \tau_a}\right)_\lambda$ |   |

seen in the three different wavelength curves, is difficult to unambiguously detect since it occurs at values of  $\tau_f$  near  $\tau_c$ ; because  $\tau_c$  is typically quite small the computation of  $\alpha'$  for small  $\tau_f$  becomes quite sensitive to interband errors in  $\tau_a$ .

The spectral derivative  $\alpha'$  is composed of the "Ångström term" which tends toward zero at large  $\tau_a$  and the weighted mean term  $(\eta\alpha'_f + (1 - \eta)\alpha'_c)$  in Table 1) which tends toward  $\alpha'_f$  in the presence of large  $\tau_a$  (for the case of an influx of fine mode particles). An important effect of the coarse fraction is that the negative Ångström term increases the influence of this mode to values of  $\tau_a$  beyond the point where the weighted mean term is significant. If we associate significant changes in  $\alpha'$  to differences which are about 10% of the asymptotic limit of  $\alpha'$  at large  $\tau_a$  (i.e.  $\alpha'_f$ ) then the weighted mean term is important to values of  $\eta$  around 0.9 (or  $\tau_f/\tau_c \sim 9$ ) while the Ångström term, because of the large  $(\alpha_f - \alpha_c)^2$  factor and given that  $\alpha'_f \sim (3/4)\alpha'_f$  is significant until about  $\eta$  near 0.96 (or  $\tau_f/\tau_c \sim 24$ ).

### 3.3. Detectable Curvature

Questions about the information content of spectral optical depth measurements can be approached by investigating polynomial fits to simulated Mie data perturbed by typical measurement errors. The general spectral expression for aerosol optical depth can be written as

$$\ln \tau_a = a_0 + a_1 \ln \lambda + a_2 \ln^2 \lambda + a_3 \ln^3 \lambda + \dots,$$

where the classical first-order Ångström relation includes only the  $a_0$  and  $a_1$  terms. Bimodal, lognormal-based Mie simulations and best fit  $\ln(\tau_a)$  polynomials were produced over a range of aerosol abundances (over a range of values of  $\tau_a$  (500 nm) between 0.01 and 0.64. Before applying the polynomial fits, the computed aerosol optical depths were perturbed by random, normally distributed errors characterized by various root-mean-square (rms) magnitudes. The spectral derivatives  $\alpha$  and  $\alpha'$  were then computed from the noise perturbed polynomials.

The differences between the optical depths computed from these polynomials and the exact bimodal (Mie) optical depths were then averaged, first over a sampling of spectral  $\tau_a$  vectors modified by random errors, then over wavelength and, finally, over abundance to produce plots of rms differences versus polynomial order. The left-most graph of Figure 4 shows the variation of these rms normalized differences  $(\Delta \tau_a / \tau_a)_{\text{rms}}$  for polynomials restricted to a typical Sun photometer spectral region between 0.35 and 1.05  $\mu\text{m}$ . The differences  $\Delta \alpha$  and  $\Delta \alpha'$  between the derivatives computed from the polynomials and the derivatives of the bimodal (Mie) optical depth curves are shown in the middle and right-most curves. The bimodal, lognormal (U.S. mid-Atlantic) case of Plate 1 was selected for this simulation exercise inasmuch as it represents a severe type of bimodal curvature.

The figure demonstrates the trade-off between the influence of pure regression errors ( $\sigma(\tau_a) = 0$ ) and the measurement noise errors. At low orders, regression error typically dominates, and there is a distinct advantage to increasing the polynomial

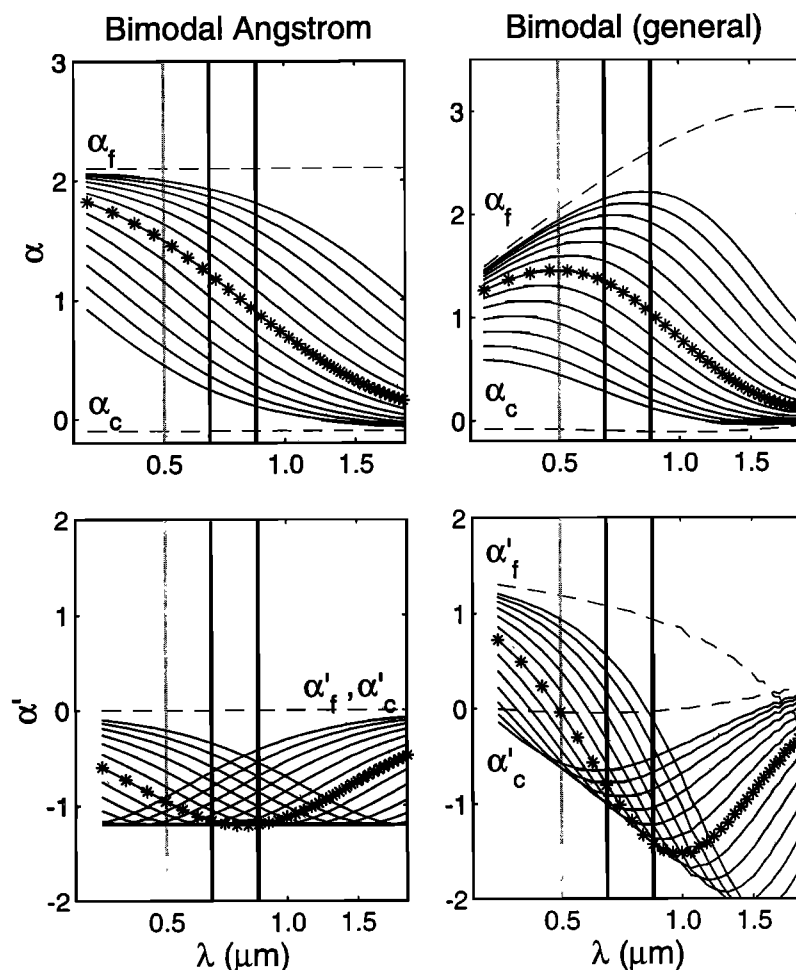


**Figure 2.** Spectra of  $\alpha$  and  $\alpha'$  (logarithmically scaled wavelength) for the case of fine and coarse Angstrom modes (left side) and fine and coarse general modes (right side). Asterisk curves correspond to the curves of Figure 1. The vertical lines are specific wavelengths whose representation in optical depth space are shown in Figure 3 (light grey, 500 nm; medium grey, 650 nm; dark grey, 850 nm). The lognormal size distributions referred to in the caption to Figure 1 were employed to represent the general bimodal case.

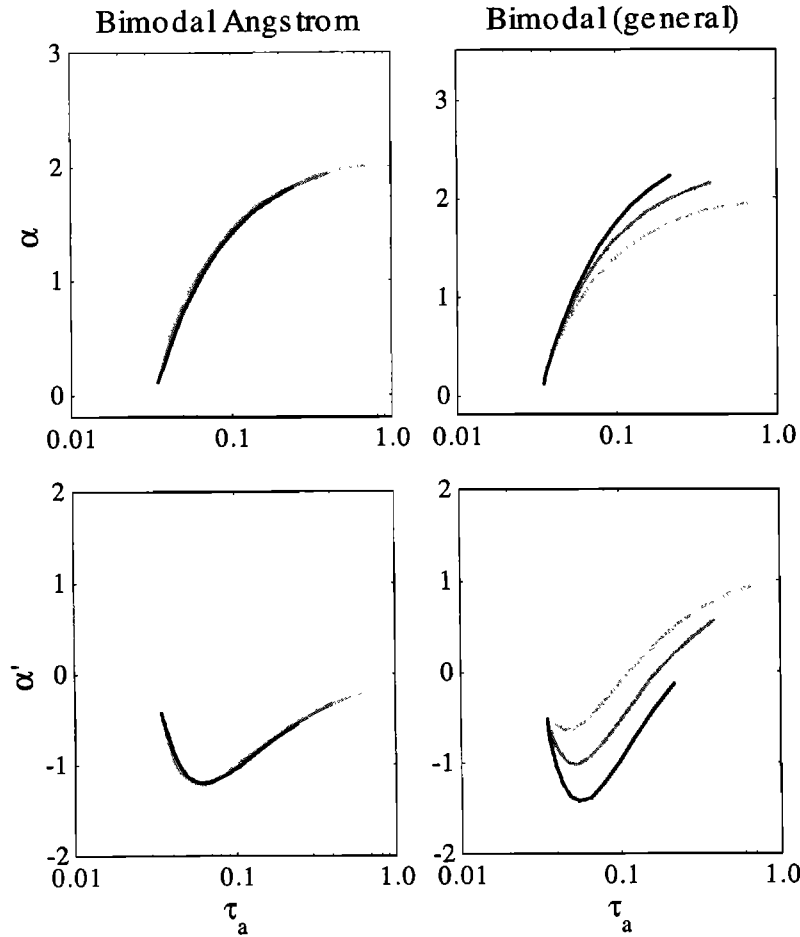
order. As the order increases, the regression errors become inconsequential compared to noise-induced errors; the latter actually increase with order since more, higher-frequency (noisy), spectral features can be accommodated by higher-order polynomials. A minimum rms difference is thus defined at a polynomial order where these two error sources balance. The dependence of the noise-induced error on polynomial order demonstrates the filtering capabilities of low-order polynomials and the effective noise reduction which can be achieved by compromising with spectral fidelity.

Figure 4 thus suggests that within the visible and NIR wavelength range a second or third order polynomial fit would encompass any possible Mie type of variation which could be detected by a standard Sun photometer with instrumental rms measurement errors of better than 0.01 in  $\tau_a$ . Since the third-order rms differences are of about the same magnitude as the second-order differences, it is advantageous to use the former if the goal is to detect more subtle spectral variations. It is worth noting here that a second or a lower-order polynomial necessarily yields a constant  $\alpha'$  which excludes any systematic variation of this parameter in spectral space. Section 4 incorporates a number of illustrations which demonstrate that

there are systematic wavelength variations in  $\alpha'$  which can be detected after effectively filtering optical depth data by means of a third-order spectral polynomial in the visible and NIR (or a higher-order polynomial in the case of the visible, NIR, and short wave infrared (SWIR)).

#### 4. Illustrations With Real Data

In the previous sections, analytical expressions for the spectral derivatives of bimodal distributions were derived, and the significance of these expressions in spectral and optical depth space was illustrated with Mie simulations. In this section we give examples of how the simple physics represented by these analytical expressions can influence measured optical depth spectra. Interband variability due to uncertainties in aerosol optical depth must first be understood in order to appreciate the significant spectral phenomena which one can hope to observe; simple concepts are given below along with a real example that underscores the sensitivity of the derived spectral parameters to unfiltered data. An example with real diurnal data is then presented in order to illustrate, in reference to the previous sections, the types of features in spectral and



**Figure 3.** Curves of  $\alpha$  and  $\alpha'$  as a function of  $\tau_a$  for the case of fine and coarse Angstrom modes (left side) and the fine and coarse general modes (right side). These curves are the projections in optical depth space of the families of  $\alpha$  and  $\alpha'$  curves seen in Figure 2 at the three wavelengths indicated by the vertical bars (light grey, 500 nm; medium grey, 650 nm; dark grey, 850 nm).

optical depth space which one can observe and explain. A second example with an ensemble of Sun photometer measurements acquired over a year is then presented in order to illustrate how the behavior of  $\alpha$  and  $\alpha'$  in optical depth space can be largely understood in terms of the bimodal expressions of section 2. Finally, an example of a thin cloud event shows how the bimodal interpretation extends to the case of cloud-induced variations in the spectral derivatives.

#### 4.1. Interband Variability

Spectral curvature is difficult to measure since it represents a second or third-order effect in a  $\ln \tau_a$  versus  $\ln \lambda$  curve. For two neighboring wavelengths it can be easily shown that the relative error in  $\alpha$  is given by the approximate expression

$$\frac{\Delta \alpha}{\alpha} \equiv \frac{\Delta \tau_a}{\delta \tau_a} - 1 = \frac{(\Delta \tau_a)_{net}}{\delta \tau_a}, \quad (9a)$$

where  $\Delta \tau_a$  and  $\delta \tau_a$  are illustrated in Figure 5 and  $(\Delta \tau_a)_{net} = \Delta \tau_a - \delta \tau_a$  is the net departure from the true difference  $\delta \tau_a$ . The difference  $\delta \tau_a$  is the true (Mie) change in optical depth between the two wavelengths, while  $\Delta \tau_a$  is the measured difference. The

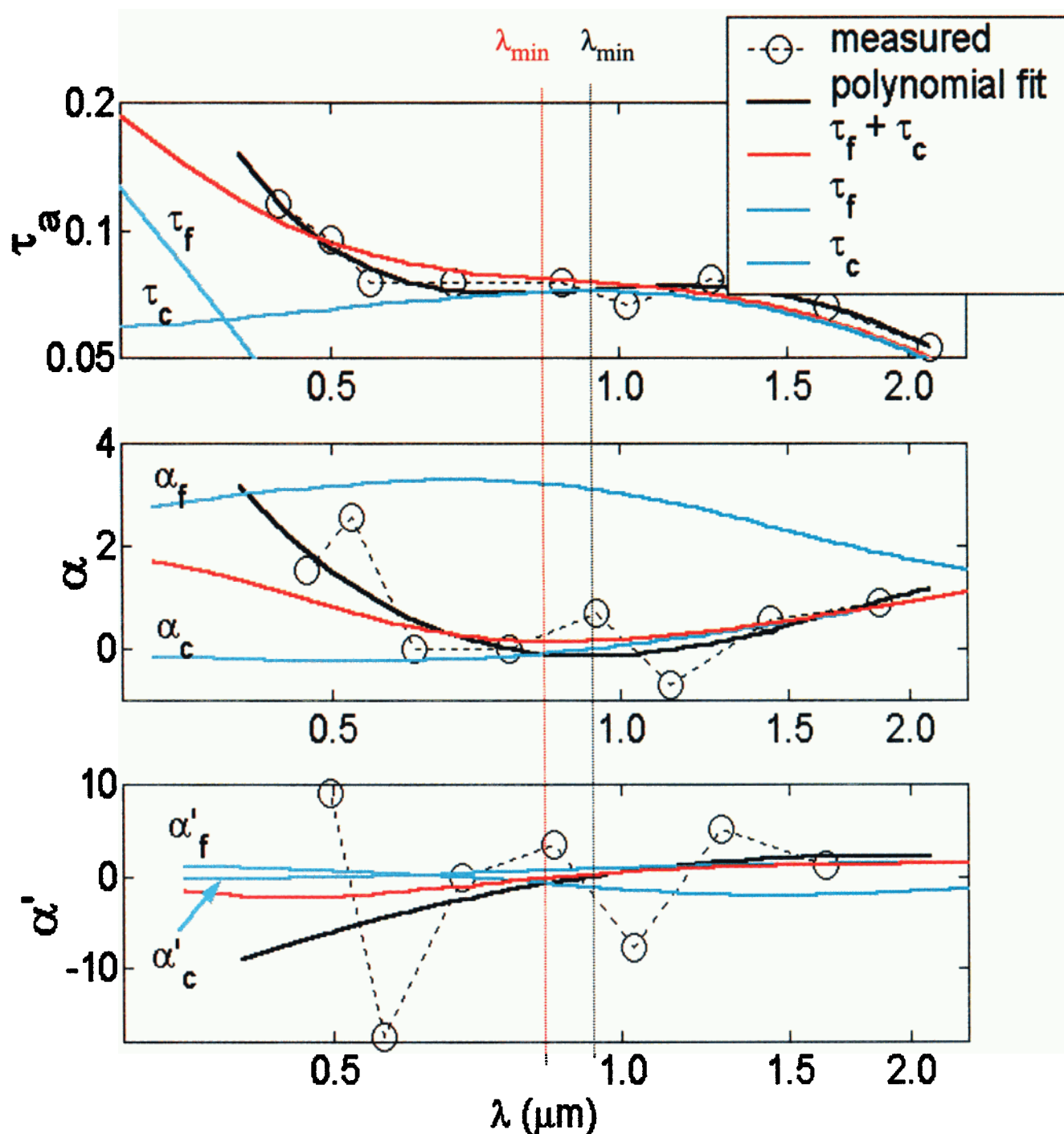
magnifying effects of the error in an  $\alpha$  versus  $\ln \lambda$  computation are evident from equation (9a); small values of  $\delta \tau_a$  for neighboring wavelength pairs can easily generate large values in  $\Delta \alpha$ ; as optical depths decrease the instrumental (interband) error portion of  $(\Delta \tau_a)_{net}$  remains roughly fixed, while  $\delta \tau_a$  decreases as  $\tau_a$  (as the product  $\tau_a \alpha \Delta \ln \lambda$ ).

The approximate slope error expression above applies equally well to  $\alpha'$ ;

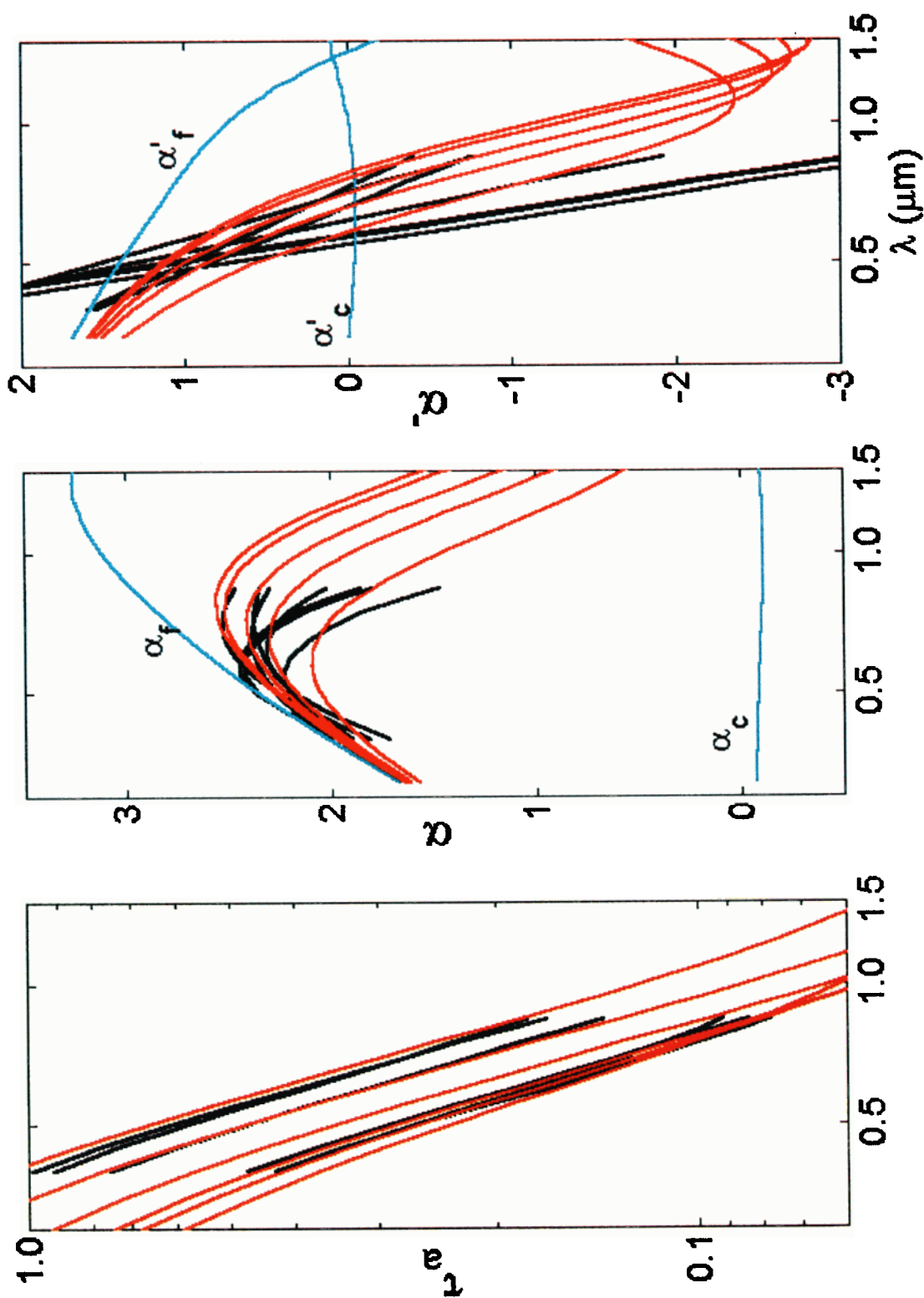
$$\frac{\Delta \alpha'}{\alpha'} \equiv \frac{(\Delta \alpha')_{net}}{\delta \alpha'}. \quad (9b)$$

Plate 1 illustrates the sensitivity of the spectral curvature parameters  $\alpha$  and  $\alpha'$  (middle and bottom graphs) to interband deviations from the type of smooth spectral variation observed in the Mie examples of Figures 1 and 2. The circles represent real data, while the solid red curve is a Mie fit using cross sections derived for fine and coarse mode lognormal distributions. The lognormal bimodal components employed in this figure were not obtained by any formal inversion scheme but rather were selected in a trial and error type of approach (the lognormal parameters were taken from selections in the look-up table of Tanré *et al.*, [1999]. The black curve in the top graph is





**Plate 1.** Spectra of  $\tau_a$ ,  $\alpha$  and  $\alpha'$  for CIMEL and MODIS Airborne Simulator (MAS) data acquired in 1996 [Tanré et al., 1999] compared to a bimodal lognormal case where the fine fraction optical depth at 500 nm was 0.028, and the coarse mode optical depth at 500 nm was taken as 0.065. The refractive index,  $r_N$ , and  $\sigma$  for the fine mode were taken as  $1.43 - 0.0035i$ ,  $0.035 \mu\text{m}$  and 1.5, respectively and  $1.44 - 0.0035i$ ,  $0.4 \mu\text{m}$  and 1.8 for the coarse fraction (seasalt) mode. The solid black line in the top curve is a fourth-order polynomial fit while the solid curves in the second and third figures from the top are the first and second-order derivatives of this curve. The cyan curves represent the individual modes.



**Plate 2.** Spectra of  $\tau_e$ ,  $\alpha$  and  $\alpha'$  (black curves) for CIMEL data acquired during the event referred to in Figure 6 compared to a bimodal lognormal case derived from Mie calculations (red curves). The black curves representing the Sun photometer data are best-fit third-order polynomials. The refractive index, lognormal geometric mean radius ( $r_N$ ) and lognormal  $\sigma$  for the fine fraction were taken as 1.43 - 0.0035i, 0.075  $\mu\text{m}$  and 1.5, respectively while the analogous parameters for the coarse fraction were 1.5 - 0i, 0.5, and 2.5, respectively. The cyan curves represent the individual modes.

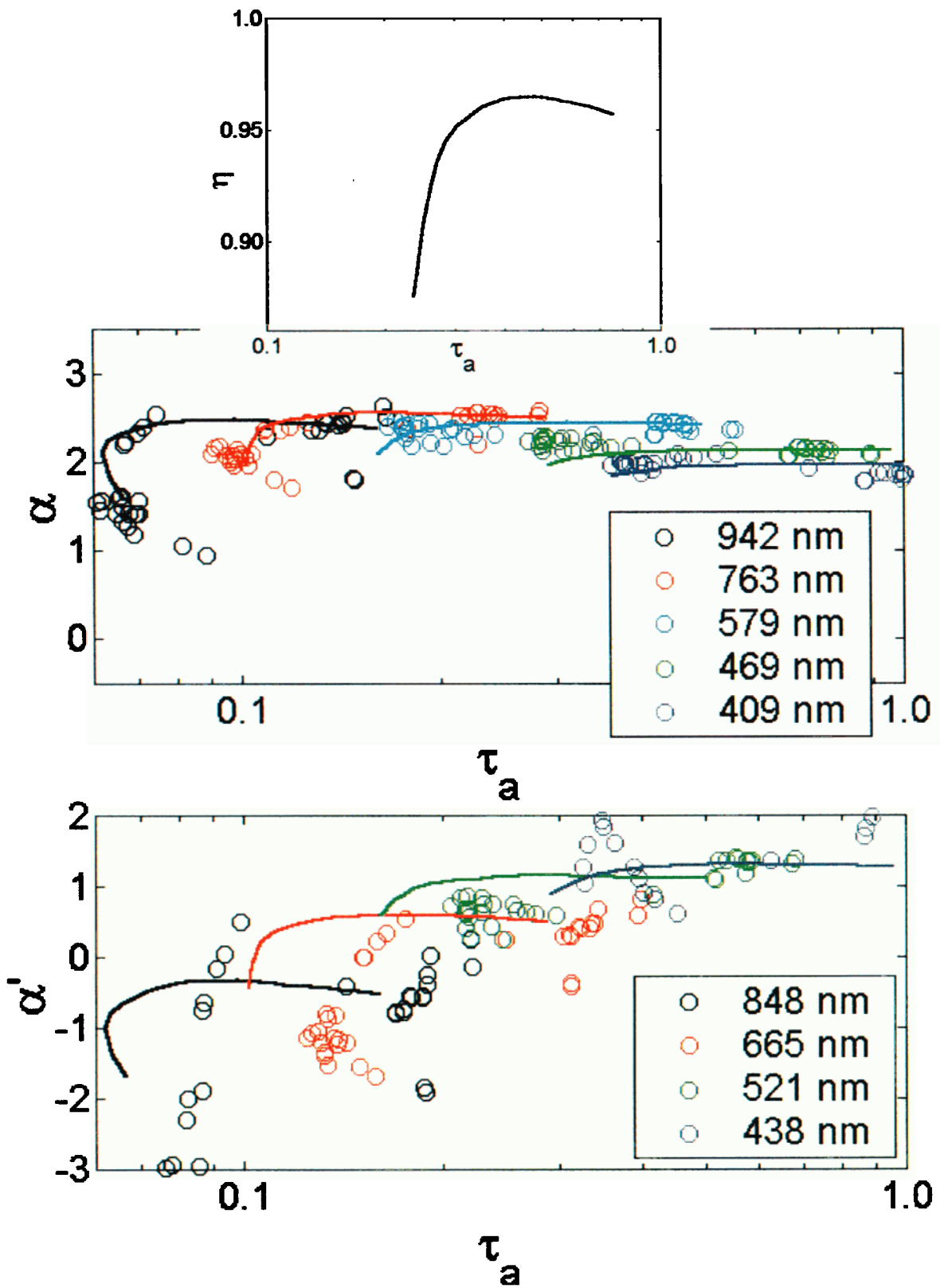


**Plate 3.** Values of  $\alpha$  and  $\alpha'$  versus  $\tau_a$  for the data and simulations of Plate 2. The fractional evolution of the fine mode as a function of  $\tau_a$  at 500 nm wavelength is described by  $\eta$  in the small inset figure. This curve was also used to generate all the bimodal lognormal (red) curves of Plate 2.

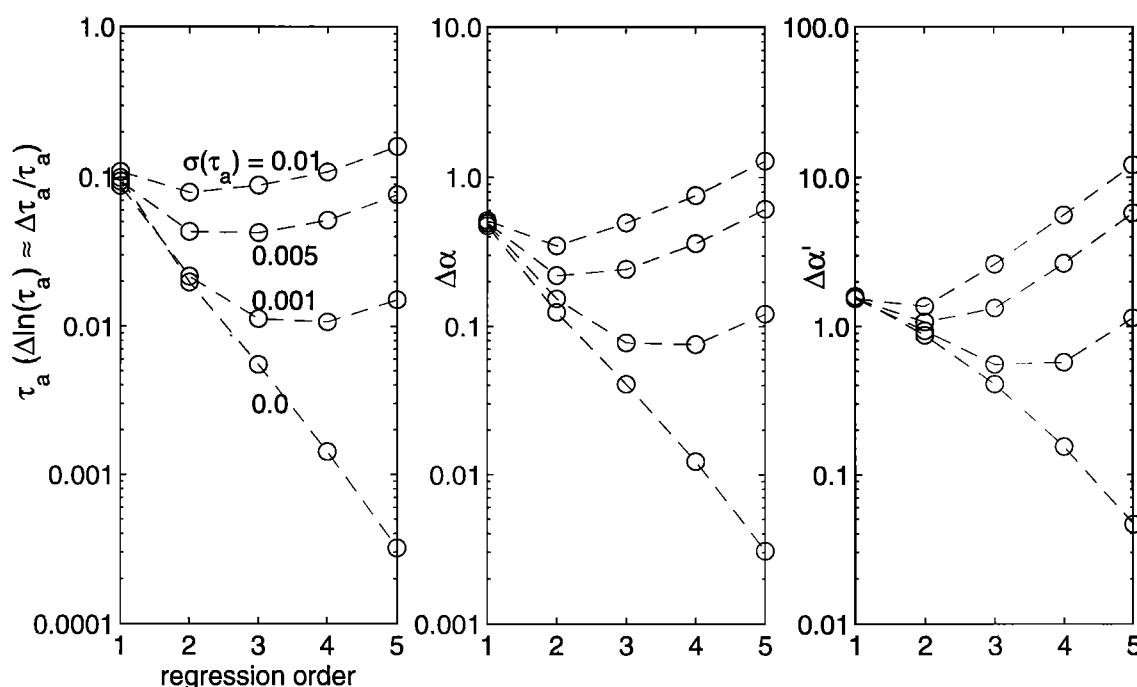


**Figure 4.** Wavelength and optical depth-averaged fitting errors in the spectral range of 350 to 1050 nm as a function of the degree of spectral fitting polynomials. The fine mode optical depth  $\tau_a(500 \text{ nm})$  was allowed to increase from 0.01 to 0.64 by factors of  $\sqrt{2}$ , and  $\tau_c(500 \text{ nm})$  was fixed at 0.03. Random, normally distributed errors characterized by a standard deviation (the  $\sigma(\tau_a)$  labels near each curve) were added to the nominal  $\tau_a$  values. The lognormal size distributions described in Plate 1 caption were used to generate this figure.

a fourth-order regression polynomial fit through the measured optical depth data, while the successive derivatives of this curve are shown in the middle and bottom graphs. An analysis similar to the VIS and NIR simulations of section 3.3 indicated that a fourth-order polynomial would be advantageous for the larger spectral region encompassing the visible and shortwave infrared spectral region (0.35 to 2.5  $\mu\text{m}$ ). It is emphasized that the spectral range of Plate 1 was chosen to attain maximum spectral curvature for the purposes of illustration; the spectral range and the polynomial order in all the other examples in this paper correspond to the conditions used to generate Figure 4 (0.35 to 1.05  $\mu\text{m}$  and third order).

One can observe that rather small departures from the smooth optical depth curves in the top graph are effectively magnified in

the bottom curves and that in particular,  $\alpha'$  is very much distorted relative to the bimodal curve. At the same time, the derivatives of the fourth-order polynomial fit effectively reduce the impact of the deviations from smooth spectral optical depth and yield results which are significantly more consistent with the bimodal curves.

#### 4.2. Spectral Space

Plate 1, in addition to serving as a good illustration of the effects of unfiltered interband errors on spectral curvature, provides an interesting curvature example that can be viewed as a variant of Figure 1. The Mie curves, selected to model this spectrum correspond to a relatively small fine particle mode

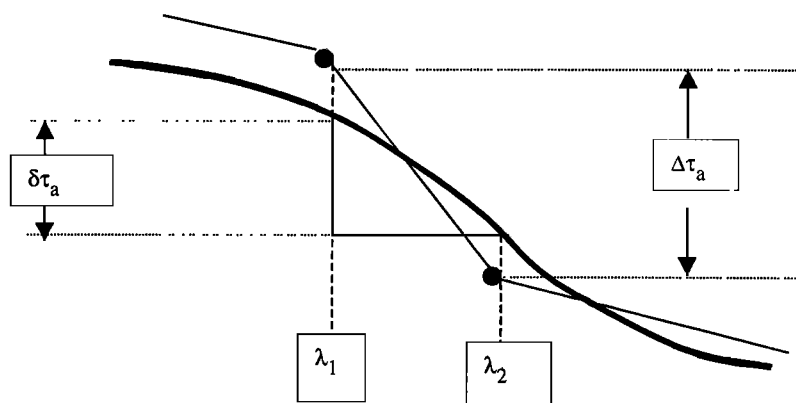


**Figure 5.** Diagram illustrating the influence of intraband optical depth error on the estimate of  $\alpha$  (in support of equation (9a)).

with an effective radius ( $r_{eff}$ ) of  $0.053 \mu\text{m}$  and a small coarse particle (sea salt) mode with an effective radius of  $0.95 \mu\text{m}$  (see the Notation section for a definition of effective radius). In effect the peak in  $\alpha_f$  and an analogous peak in  $\alpha_c$  are shifted toward the left relative to the case presented in Figure 1 (the latter peak is at longer wavelengths than appear in that figure). A minimum results because of the decrease in  $\alpha$  brought about by the averaging effects discussed in section 3.1.1 (when  $\tau_f \sim \tau_c$ ) and the increase in  $\alpha$  brought about by the spectral curvature in  $\alpha_c$  after the peak in  $\tau_c$  near  $1 \mu\text{m}$ . Plate 1 is analogous to Figure 1 in that it shows the case of an extrema in  $\alpha$  (zero in  $\alpha'$ ) as well as an inflection in  $\alpha$  (minimum in  $\alpha'$ ) although the latter cannot be seen in the spectrum of the real data.

**4.2.1. Diurnal variation example.** Figure 6 shows the temporal variation of  $\tau_a(763 \text{ nm})$  and  $\alpha(763 \text{ nm})$  for cloud-screened Sun photometer data [Smirnov *et al.*, 2000] collected during a diurnal optical depth event on July 13, 1997, at the Goddard Space Flight Center (GSFC) NASA in Greenbelt, Maryland. The spectral behavior of  $\tau_a$  before and after its significant and abrupt increase at around 1900 UT (UT/24 = 0.8) was chosen as another case study which would illustrate the bimodal influence in spectral and optical depth space. The 763 nm wavelength employed in Figure 6 was chosen to demonstrate the temporal variability since the bimodal influence of the coarse mode on  $\alpha$  is much more in evidence in the NIR. The optical depth spectra associated with this diurnal event are the basis of the illustrations in spectral and optical depth space given in Plates 2 and 3 below.

The middle graph of Plate 2 shows a set of spectral maximums in  $\alpha$  corresponding to a set of zeros in  $\alpha'$  for selected spectra; the solid black curves correspond to the diurnal event of Figure 6 after the optical depth spectra have been smoothed by a third-order polynomial, while the solid red curves were generated using bimodal combinations of the two modes given in the figure caption. For clarity, only a selection of representative polynomial fits to the measured data are displayed. The procedure for generating the red bimodal simulation curves was to find an  $\alpha_f$  value that could be employed as an upper envelope of all measured  $\alpha$  curves and then, by trial and error, to select appropriate  $\eta$  and  $\tau_a$  values which simulated the major spectra groupings of the measured  $\tau_a$ ,  $\alpha$ , and  $\alpha'$  curves (as well as the behavior in optical depth space discussed below in section 4.3.1). Spectral variations of  $\alpha'$  in the form of a systematic decreasing trend and wavelength-dependent zero intercepts are expected from the red curve simulations and can be detected in the smoothed data curves. The grouping in the polynomial data of large-slope linear decreases in  $\alpha'$ , which are not well represented by the red curve simulations, represent narrow spectral features in  $\alpha$  whose  $\alpha_f$  curve could only be explained by rather narrow size distributions or by admitting the possibility of small but spectrally systematic errors in optical depth.

This example demonstrates that third-order spectral curvature can be detected across small to intermediate magnitude  $\tau_a$  spectra limited to the visible and NIR region. It should be understood that constraining the  $\ln \tau_a$  versus  $\ln \lambda$  polynomial fit to second order necessarily means that  $\alpha'$  is a constant, and for example, the zero crossings of the  $\alpha'$  curves of Plate 2 could not be reproduced. The spectral behavior of the curves with increasing wavelength was already noted in the case of Figure 1 as an optical depth averaging effect between the competing

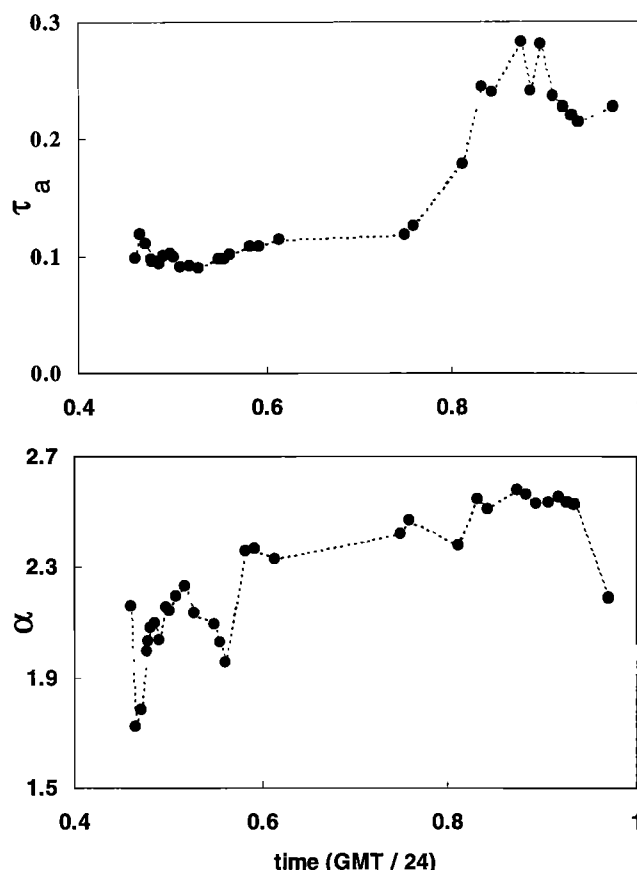


**Figure 6.** Optical depth and Angstrom coefficient variation (763 nm) as a function of time for cloud-filtered CIMEL data acquired during a diurnal optical depth event (July 13, 1997, at the GSFC NASA site in Greenbelt, Maryland). The data have not yet been smoothed with a spectral polynomial.

influences of increasing  $\alpha_f$  and the small, relatively constant values of  $\alpha_c$ .

### 4.3. Optical Depth Space

**4.3.1. Diurnal variation example.** Plate 3 shows measured values of  $\alpha$  and  $\alpha'$  in optical depth space (circles) compared to curves generated from a superset of the bimodal components and optical mixing ratios ( $\eta$ ) employed in the spectral simulations of Plate 2 (the small insert figure shows the value of  $\eta(500 \text{ nm})$  employed to generate the simulated curves of Plates 2 and 3). The general trend, with some obvious large outliers, is reproduced in the  $\alpha$  curves, while the comparison between simulations and measurements in the  $\alpha'$  curves, although influenced by the types of problems seen in Plate 2, still shows a qualitative agreement. This example incorporates some of the spectral and optical depth space aspects discussed in sections 3.1 and 3.2 while at the same time illustrating a case of apparent diurnal nonlinear changes in  $\eta$  induced by simultaneous changes in  $\tau_f$  and  $\tau_c$ .

**4.3.2. Statistical ensemble.** An ensemble of 1998 optical depth data (910 spectra) was acquired at the GSFC NASA station belonging to the AERONET network of CIMEL Sun photometers [Holben *et al.*, 1998]. The CIMEL Sun photometer operates in seven spectral bands (340, 380, 440, 500, 675, 870,

and 1020 nm plus a 940 nm water vapor band) and periodically scans off the solar disk to acquire sky radiance data. The optical depths were measured by two reference Sun photometers (101 and 37) whose optical depth accuracy at all wavelengths was believed to be better than 0.01. These two Sun photometers had been calibrated at the Mauna Loa Observatory 4 times and 3 times respectively during the 1998 season. The cloud-screening algorithm of *Smirnov et al.* [2000] was applied to these data.

Comprehensive particle size and refractive index inversions using near simultaneously measured optical depths and hemispherical almucantar sky radiances at four wavelengths (440, 675, 860, 1020) were applied to these data according to the procedure developed by *Dubovik and King* [2000]. A total of 930 inverted particle size distributions were divided into fine and coarse modes at approximately 0.6  $\mu\text{m}$  radius. Figure 7 shows the resulting particle size distribution inversions subdivided into 15 classes obtained by averaging the retrieved distributions into bins of 62 measurements ordered according to increasing  $\tau_a$  (1020 nm).

A general bimodality can be observed in the curves of Figure 7 accompanied by significant variations in the features of the individual distributions. The increase of the peak radius of the fine mode distribution with increasing aerosol optical depth is significant and leads to systematic spectral curvature features which translate into significant variations in  $\alpha$  (see the discussion associated with Figure 8 below). The presence of a second weaker coarse particle mode at around 2  $\mu\text{m}$  for intermediate  $\tau_a$  means that the representation of supermicron

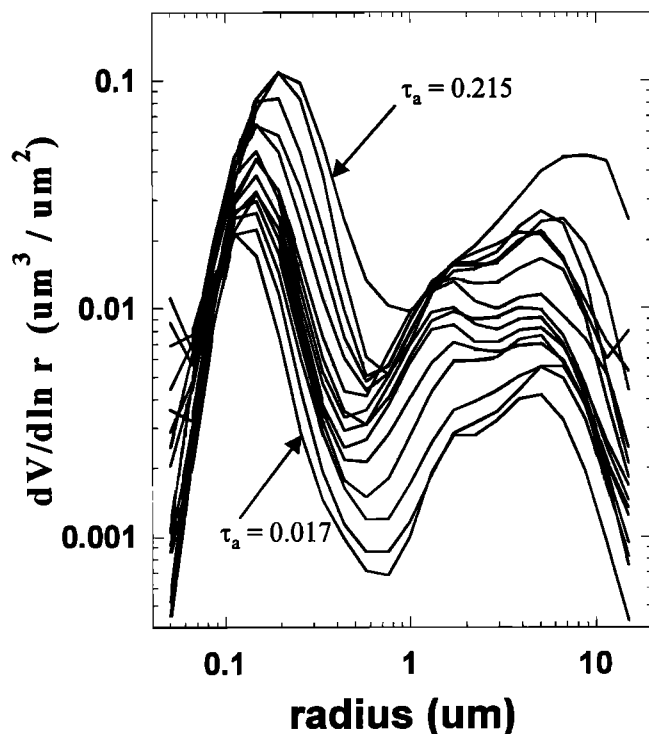


**Figure 7.** Particle size distribution inversions for 930 sets of 1998 GSFC almucantar and  $\tau_a$  data. The inversions results were averaged over equal numbers of measurements (ordered according to increasing  $\tau_a$ ) to form the 15 separate classes seen in this graph. The inversion procedure is described by *Dubovik and King* [2000].

**Table 3.** Optical Depth Statistics for the 1998 GSFC Data Set (Interpolated to 500 nm)

|          | Log Distribution Parameters | Optical Depths Corresponding to the Mean and Standard Deviations (sd) of the Log Distributions |                          |                          |
|----------|-----------------------------|--|--------------------------|--------------------------|
|          |                             | $\langle \log(\tau) \rangle \pm \text{sd}$   | $\log(\tau) - \text{sd}$ | $\log(\tau) + \text{sd}$ |
| $\tau_f$ | $-0.74 \pm 0.35$            | 0.0811   | 0.1816                   | 0.4064                   |
| $\tau_c$ | $-1.80 \pm 0.29$            | 0.0079   | 0.0158                   | 0.0316                   |
| $\tau_a$ | $-0.70 \pm 0.35$            | 0.0885   | 0.1982                   | 0.4436                   |

The logarithms are to the base 10.

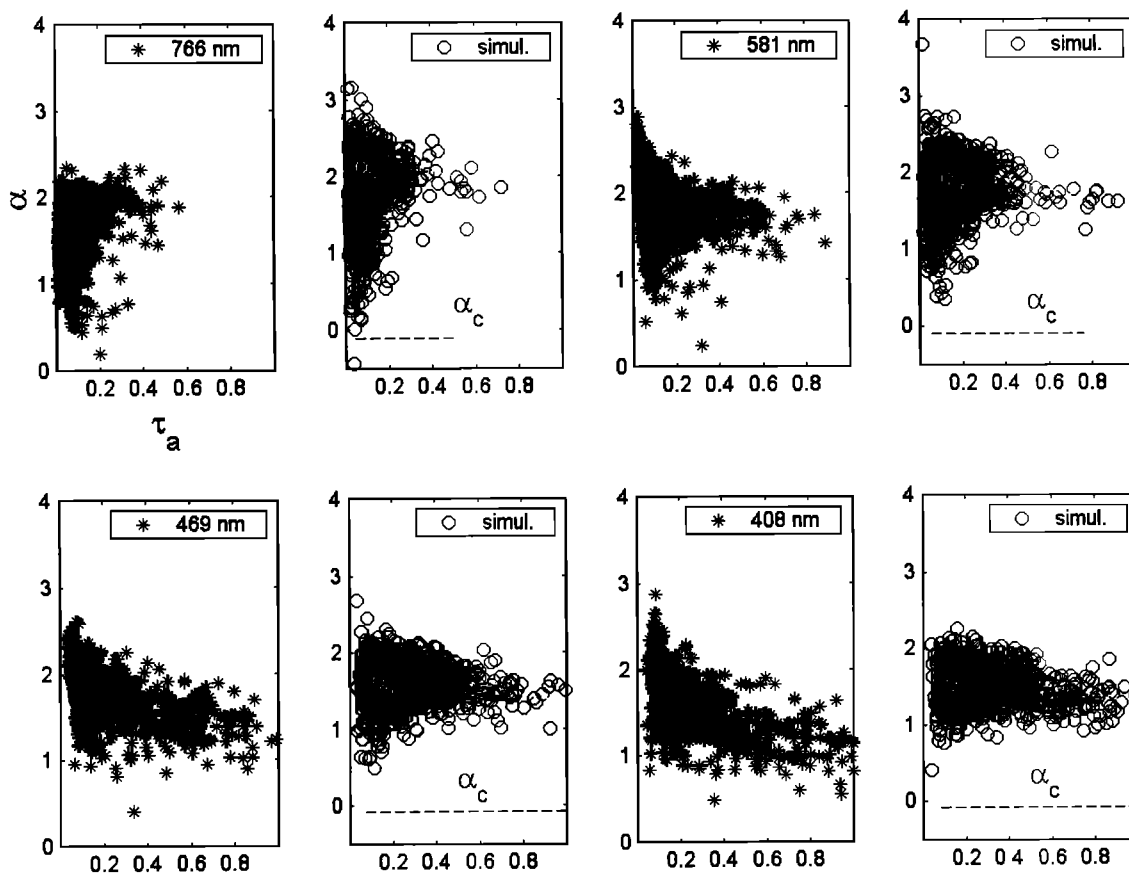
particles by a single mode necessarily implies a forced averaging of this range of particles sizes. It should be noted that the presentation of these curves is somewhat deceiving in terms of optical effects since the principal optical contribution (the volume extinction coefficient) is the product of the differential volume size distribution of Figure 7 and an optical kernel which is strongly influenced by a  $1/r$  multiplicative term (see, for example, *Hansen and Travis* [1974]). The overall optical depth statistics derived from the separate modes of Figure 7 yielded the logarithmically based results shown in Table 3.

Figure 8 shows four pairs (four wavelengths) of  $\alpha$  versus  $\tau_a$  graphs which permit side-by-side comparisons between measurements from the 1998 data ensemble and simulations using equations (4) and (5) and a normally distributed random number generator to represent the natural variation in  $\log(\tau_f)$  and  $\log(\tau_c)$  (constrained by the means and standard deviations given in Table 3). Figure 9 shows three pairs of  $\alpha'$  versus  $\tau_a$  graphs which compare the 1998 data with simulations (at three different wavelengths). The random number generator was used to produce distributions of  $\tau_f$  and  $\tau_c$  at 500 nm, and these values, along with fixed  $C_p$ ,  $C'_p$ ,  $\alpha_p$ ,  $\alpha'_p$ ,  $\alpha_c$ , and  $\alpha'_c$  values, were subsequently used to generate ensembles of  $\alpha$  and  $\alpha'$  values. The details of the simulations and the parameters employed are given in Table 4 and Figures 10 and 11. In what follows we give an overview of the line of reasoning which led to the final procedure used in producing the simulations in Figures 8 and 9.

It is noted that a correlation was observed between the fine and coarse mode optical depths ( $\tau_c \sim 0.064 \tau_f$  at 500 nm). However, this correlation, in comparisons with the fixed means and standard deviations of Table 3, did not significantly alter the general appearance of the simulated graphs in Figures 8 and 9.

One can observe that the general features of the  $\alpha$  and  $\alpha'$  behavior in optical depth space are captured by the bimodal simulations. It was necessary, however, to make supplementary assumptions beyond the simple normal distributions in  $\log(\tau_f)$  and  $\log(\tau_c)$  in order to simulate all the observable trends in the real data. The initial  $\alpha$  simulations based on equation (4) could not duplicate the gradual decrease in  $\alpha$  with increasing large  $\tau_a$  at the shorter wavelengths unless (1) a significant increasing coarse mode influence with increasing optical depth was simulated or (2) the fine mode was allowed to evolve and increase in size as the aerosol optical depth increased.

The correlation noted above between  $\tau_f$  and  $\tau_c$  was too weak to induce the decreasing  $\alpha$  trend in the measured distributions of Figure 8. The second hypothesis is readily simulated and has a physical justification; the bimodal accumulation mode observations of *Remer et al.* [1999] and our own inversion



**Figure 8.** Plots of  $\alpha$  versus  $\tau_a$  for the 1998 GSFC  $\tau_a$  data (the four graphs with asterisks) side by side with simulations performed according to the detailed steps given in Table 4 (the four graphs with open circles). The four measurement wavelengths are the center (log) wavelengths for each differential calculation (differentials applied to the original Sun photometer wavelengths). This choice of wavelengths was more an artifact of data processing heritage because the polynomial fitting approach permits any choice of wavelength. The simulated data result from Mie computations at a resolution of 50 nm and hence the wavelengths of the simulation graphs are the nearest multiple of 50 to the measured wavelengths.

results indicate a general increasing trend of the average fine mode particle size with  $\tau_a$  (see Figure 7). To account for this in terms of the bimodal computations, we modeled the fine mode behavior using a gradual evolution as a (linear) function of  $\tau_a$  between the values of  $\alpha_f$  computed for the small and large accumulation mode models which Remer et al. termed ACC-1 and ACC-2, respectively (the same type of linear function was used for  $\alpha'_f$ ). This fine mode evolution produced the correct decreasing trend in  $\alpha$  but not the rather large vertical spread of  $\alpha$  values at a given large value of  $\tau_a$ . The adjustment, which satisfactorily mimicked the vertical spread, was to permit a certain random element in the  $\alpha_f$  upper limit (i.e., one must concede a small natural variation in the mode size distribution at a given value of  $\tau_a$ ).

It is worth noting that the particle size distribution inversions of Remer et al. for the 1996 east coast TARFOX campaign and the 1998 inversions of Figure 7 are remarkably consistent; the  $r_{eff}$  values for ACC-1 and ACC-2 were 0.10 and 0.19  $\mu\text{m}$ , respectively for optical depths roughly between 0.05 and 0.6 at 670 nm compared to 0.11 and 0.17 from the data of Figure 7 for optical depths between 0.02 and 0.5 at the same wavelength.

Remer et al. used a fixed refractive index of 1.43-0.0035i, while our inversions yielded refractive index as an output (values  $\sim 1.40 - 0.005i$  for all wavelengths).

Although a vertical wing structure dominates at small  $\tau_a$ , the measured data of Figure 9 show two features which are captured by the simulations: (1) a gradual increase in  $\alpha'$  with increasing (larger values of)  $\tau_a$  and (2) a more abrupt increase at smaller  $\tau_a$  which manifests itself as a greater concentration of points in the lower half of the vertical wings at larger wavelengths (this separation into vertical halves is less evident in the simulated data of Figure 9; one must reference the upper and lower wings above and below an extrapolation of the line which bisects the phalanx of points seen at larger optical depths). In the first case, the evolution of the fine particle mode with increasing  $\tau_a$  causes an increase in  $\alpha'_f$  and a corresponding increase in  $\alpha'$  for large  $\tau_a$ . In the latter case the negative Angstrom term of the  $\alpha'$  expression in Table 1 is responsible for a slow increase in  $\alpha'$  from negative to positive values over a range of small to intermediate values of  $\tau_f$  (from  $\tau_f \sim 0$  to  $\tau_f \sim 24 \tau_c$  as per section 3.2). The bottom right hand-graph of Figure 3, which shows a slow rise to asymptotic values of  $\alpha'$  under conditions of a monotonic increase in  $\tau_f$  in the presence of a small fixed  $\tau_c$ , is an illustration of this latter type of behavior.

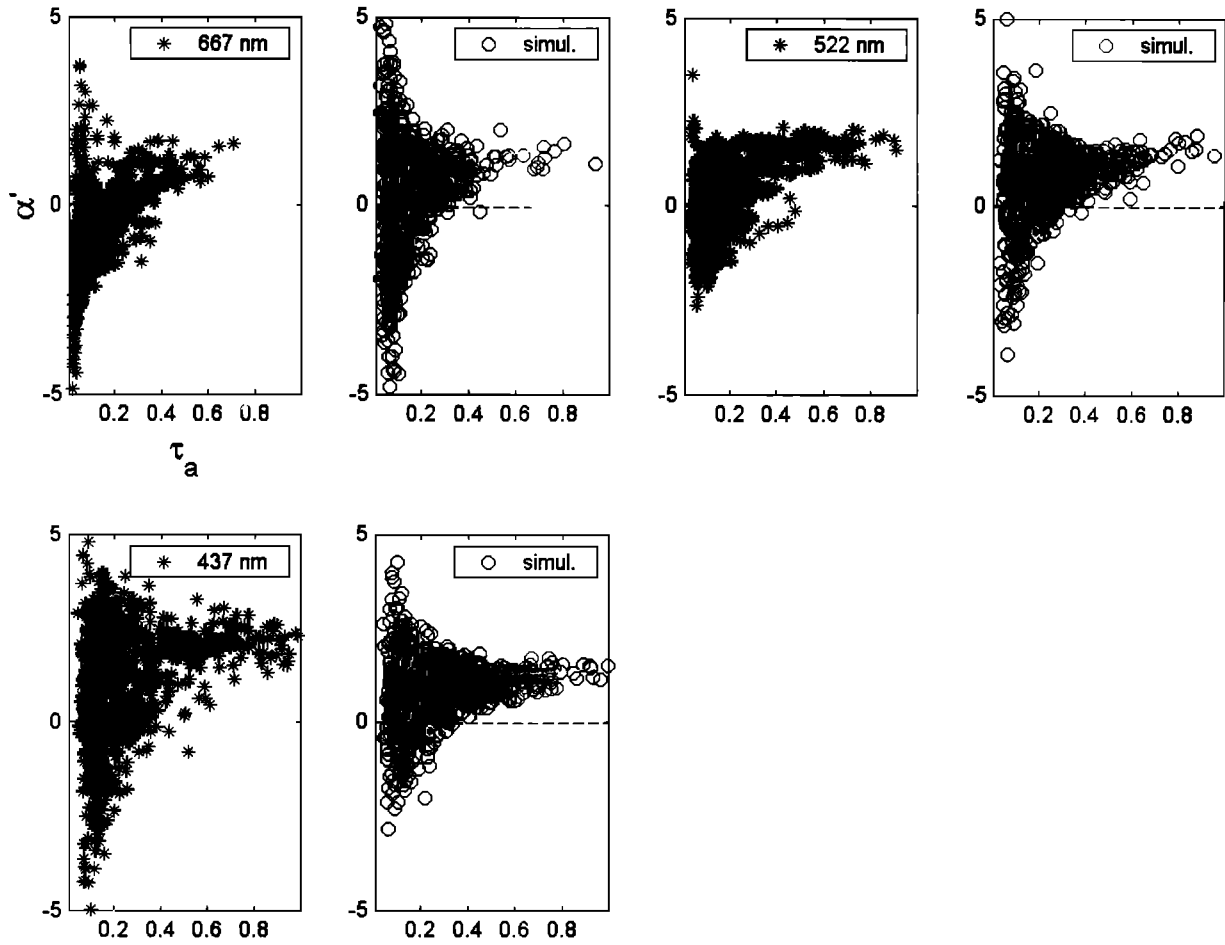


**Figure 9.** Plots of  $\alpha'$  versus  $\tau_a$  for the 1998 GSFC  $\tau_a$  data (the four graphs with asterisks) side by side with simulations performed according to the detailed steps given in Table 4 (the four graphs with open circles). See Figure 8 caption for more details.

Figure 3 (and Table 2) also predict minima in  $\alpha'$  versus  $\tau_a$  which should vary with wavelength. Such an effect appears in the simulated data as an abrupt lower boundary to the ensemble of noise-free generated points but disappears with the addition of the noise error discussed immediately below.

The vertical wings in the  $\alpha'$  curves at small optical depth (and to a lesser degree in the  $\alpha$  curves) could only be modeled by adding independent optical depth error components to the simulations. From equation (9a) and given that  $\delta\tau_a \equiv -\tau_a \Delta \ln \lambda$  and  $\delta\alpha \equiv \alpha' \Delta \ln \lambda$ , one can write approximate rms error values as

$$\Delta\alpha_{rms} \equiv \frac{1}{\Delta \ln \lambda} \frac{\sigma(\tau_a)}{\tau_a}, \quad (10a)$$

$$\Delta\alpha'_{rms} \equiv \frac{\sqrt{2}}{(\Delta \ln \lambda)^2} \frac{\sigma(\tau_a)}{\tau_a}, \quad (10b)$$

$$\Delta\alpha_{rms} \approx 3 \frac{\sigma(\tau_a)}{\tau_a}, \quad (10c)$$

$$\Delta\alpha'_{rms} \approx 20 \frac{\sigma(\tau_a)}{\tau_a}. \quad (10d)$$

where  $\sigma(\tau_a)$  is the standard deviation of a random, normally distributed set of optical depth measurements. Although these

expressions are clearly inappropriate for derivatives of polynomials fitted to spectral data they do provide an indication of the formulation required. The computations employed in the creation of Figure 4 were applied to the size distributions of *Remer et al.* [1999] to yield the relations below for third-order polynomial fits in the 0.35 to 1.05  $\mu\text{m}$  spectral region and values of  $\sigma(\tau_a)$  between 0.01 and 0.005;

These expressions were used as input standard deviations to random, normally distributed estimates of measurement errors in  $\alpha$  and  $\alpha'$ . A value of  $\sigma(\tau_a) = 0.006$  for all bands was found to yield a reasonable imitation of the vertical wings in the real data and was the value employed to produce the simulated data (the shape of the  $\alpha'$  distribution in optical depth space was not very sensitive to values between 0.006 and 0.01).

The simulation mechanisms discussed above can be more readily appreciated if they are explicitly categorized according to the five steps shown in Table 4. Figures 10 and 11 show the actual generation of simulation results at a wavelength of 450 nm in terms of the resulting  $\alpha$  versus  $\tau_a$  and  $\alpha'$  versus  $\tau_a$  graphs obtained after each of these five steps. The final graphs (Figures 10e and 11e) can be found in the second row and second column of Figures 8 and 9, respectively.

Each elemental graph thus clearly illustrates the impact of the separate simulation mechanisms on the final distributions obtained in Figures 8 and 9. One can observe the dramatic



**Table 4.** Steps in the Simulation Process Used to Generate Figures 8 and 9

| Step | Variation Added            | Description  |
|------|----------------------------|--|
| (1)  | $\tau_f$                   | Lognormally distributed random variation constrained by the statistical parameters of Table 3 and equations (4) and (5). Simulation of the contribution of the natural variation of fine mode abundance to $\tau_a$ (first term of equation (1b)). |
| (2)  | $\tau_c$                   | As per $\tau_f$ in step 1 but corresponding to the second term of equation (1b).   |
| (3)  | $\alpha_f$ and $\alpha'_f$ | The Ångström exponents $\alpha_f$ and $\alpha'_f$ are allowed to vary as a linear function of $\tau_a$ (500 nm) between the two accumulation mode extremes of ACC-1 and ACC-2 defined in the notes below.  |
| (4)  | noise in $\tau_a$          | Normally distributed random distribution about each value of $\tau_a$ contributes to noise in $\alpha$ and $\alpha'$ according to equations (10c) and (10d) with $\sigma(\tau_a) = 0.006$ for all wavelengths.                                     |
| (5)  | $\alpha_f$ and $\alpha'_f$ | Natural variance of $\alpha_f$ and $\alpha'_f$ . The standard deviations of both parameters were set equal to 0.2 for all wavelengths.   |

Steps (1) to (5) correspond exactly to the five simulation illustrations shown in Figures 10 and 11. For steps (1) and (2) the statistical parameterizations employed are detailed in Table 3. The fine and coarse mode size and refractive index parameterizations were ACC-1  $\rightarrow r_{Nf} = 0.043 \mu\text{m}$ ;  $\sigma_f = 1.8$ ;  $m = 1.43 - 0.0035i$ ; [Remer *et al.*, 1999]; ACC-2  $\rightarrow r_{Nf} = 0.1 \mu\text{m}$ ;  $\sigma_f = 1.65$ ;  $m = 1.43 - 0.0035i$  [Remer *et al.*, 1999]; coarse mode  $\rightarrow r_{Nc} = 0.5 \mu\text{m}$ ;  $\sigma_c = 2.5$ ;  $m = 1.5 - 0i$

effects of optical depth noise at small  $\tau_a$  on  $\alpha$  and in particular on  $\alpha'$ . One can also note the important influence of the variance in  $\tau_c$  and the need to include a natural variance in  $\alpha_f$  in order to achieve a significant broadening of the vertical variance in  $\alpha$  at large  $\tau_a$ . The influence of the simulated minimum in  $\alpha'$  versus  $\tau_a$  curves at small  $\tau_a$  is difficult to see at the universal scale chosen for Figures 9 and 11, but it does manifest itself as a flat lower limit of  $\alpha'$  at the smaller  $\tau_a$  values of Figure 11b.

#### 4.4. Thin Cloud Event

Figure 12 illustrates how the bimodal formulations of equations (4) and (5) can be used to describe the spectral derivatives at 500 nm wavelength in the presence of a thin cloud. If one assumes that the optically dominant thin cloud plays the spectral role of the coarse mode ( $\alpha_c \sim \alpha'_c \sim 0$ ) and given typical values of the fine mode parameters ( $\alpha_f = 2.0$  and  $\alpha'_f = 1.5$ ), then the adjustment of a time-independent value of  $\tau_f$  (500 nm) yields the estimated temporal profiles of  $\alpha$  and  $\alpha'$  shown in this figure (the best agreement using a manual approach was for  $\tau_f$  (500 nm) = 0.068). More sophisticated inversions techniques could be employed to yield a better fit. However, this simple illustration demonstrates that the bimodal formulation adequately describes the variation seen in the total

spectral derivatives  $\alpha$  and  $\alpha'$  in terms of a simple extensive variation of cloud abundance (cloud optical depth) mixed with a fixed fine mode background optical depth.

## 5. Data Processing Considerations

The analytical bimodal approach described in this paper has been investigated for a variety of cloud-screened and non-cloud-screened data sets from different AERONET stations. Although problems do appear due to the sensitivity of  $\alpha'$  to measurement errors, the bimodal approach helps to interpret the systematic behavior observed in aerosol optical depth data.

The key step in the current processing chain is the application of the third-order spectral polynomial fit to raw aerosol optical depth data at six CIMEL wavelengths (380, 440, 500, 675, 870, and 1020 nm). Residual errors between the raw data and the fitting polynomials are computed and used as indicators of the quality of the  $\alpha$  and  $\alpha'$  computations. This step helps to isolate cases where even the filtering afforded by the third-order polynomial fails to eliminate relatively strong systematic interband errors at small  $\tau_a$ . Such errors (as suggested by the type of spectral variation seen in Plate 1) have relatively little impact on estimates of  $\tau_a$  but can have moderate effects on  $\alpha$  and relatively strong effects on  $\alpha'$ . We are currently investigating a weighting scheme which weights each measurement of  $\alpha$  and  $\alpha'$  as a function of the residual polynomial fitting errors combined with the estimated measurement error.

Current investigations include the employment of equations (4) and (5) to help develop optical aerosol climatologies for certain stations in the network. Equation (6) is being used to investigate an alternative cloud-screening step which invokes the inverse relationship between  $\tau_a$  and  $\alpha$  in the presence of clouds to better identify such events in an automatic fashion. An inversion algorithm for extracting  $\alpha_f$  from  $\alpha$  and  $\alpha'$ , using equations (4) is being tested. In the future we hope to employ a similar type of algorithm for  $\alpha_c$  extraction in anticipation of the next generation of AERONET Sun photometers (whose spectral range will be extended to the shortwave infrared and thus be more sensitive to supermicron particles).

## 6. Conclusions

The behavior of the aerosol optical depth and its first and second spectral derivatives can be described in terms of the spectral interaction between the individual optical components of a bimodal size distribution. Simple analytical expressions involving the separate optical components of each mode explain virtually all the features seen in curves of  $\alpha$  and  $\alpha'$  in spectral or optical depth space.

It was demonstrated that features predicted by the analytical bimodal expressions for a fixed choice of bimodal components (fixed size distributions) could be found in measured data. These included the presence in spectral space of extrema in  $\alpha$  and zeros in  $\alpha'$ , the diurnal behavior of  $\alpha$  and  $\alpha'$  in spectral and optical depth space and the general statistical behavior of  $\alpha$  and  $\alpha'$  in optical depth space.

The analogy with basis vectors in a two-dimensional vector space is strong; the size and optical properties of each mode are fixed and the optical properties of each mode (particle cross sections and their spectral derivatives) act as basis vectors from which much of the behavior in spectral and optical depth space

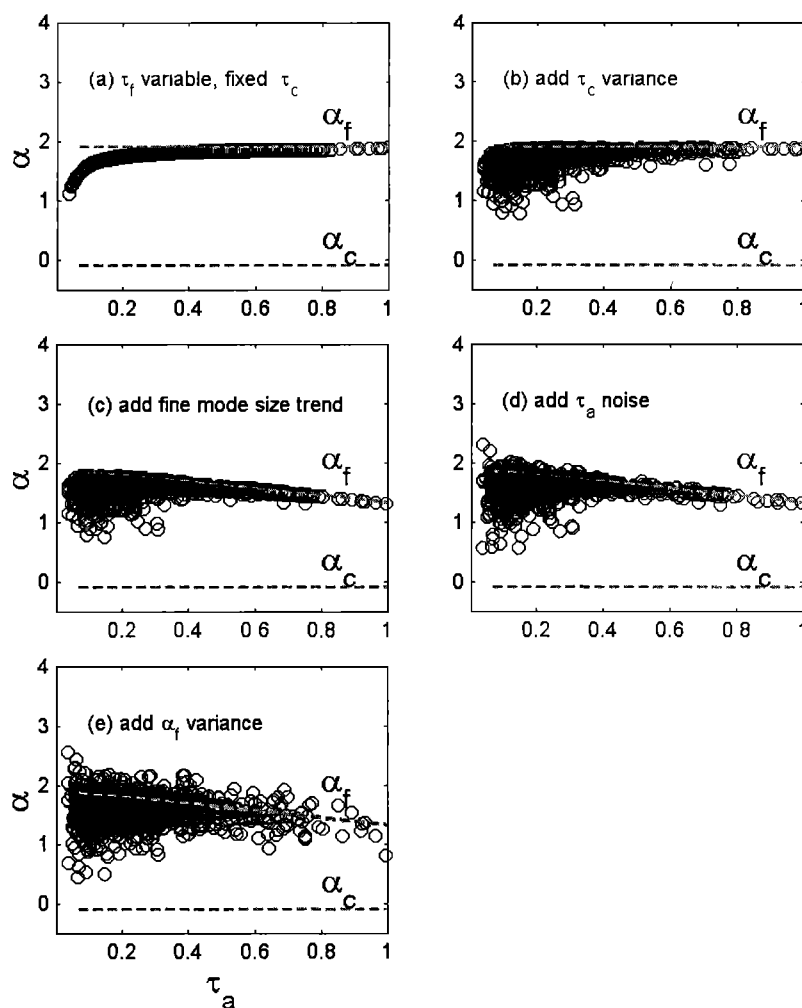


**Figure 10.** Simulated points of  $\alpha$  versus  $\tau_a$  at 450 nm wavelength showing sequential simulation steps. The final graph, Figure 10(e), corresponds to the 450 nm simulation in the second row and second column of Figure 8. Details of the simulation steps are given in Table 4.

can be generated by varying the extensive (number density dependent) contributions of fine and coarse mode optical depths. Departures from these "fixed" basis vectors would be clearly associated with differing synoptical air masses, source trajectories, and humidity conditions.

It was shown, for example, that deviations from fixed bimodal components were needed to explain certain statistical features; an increase in the fine particle mode radius with increasing  $\tau_a$  (and hence a decrease in the upper limit  $\alpha_f$  of  $\alpha$ ) had to be assumed in order to account for the gradual decrease of  $\alpha$  which occurred between moderate and large  $\tau_a$ . In addition, a small random element in the upper limit of  $\alpha_f$  had to be assumed in order to simulate the vertical spread of  $\alpha$  values at a given large value of  $\tau_a$ .

Spectral parameters are very sensitive to interband errors in measured optical depth data. Data smoothing in the form of third-order polynomial fits within the visible and NIR spectral region and fourth-order polynomial fits within the visible, NIR and short wave infrared spectral region minimize this problem and represent the limit of useful extractable information.

The bimodal spectral coefficient model can lead to simple procedures for the multiwavelength extraction of the modal

spectral coefficients and the optical mixing fraction  $\eta$  by inverting equations (4) and (5), given a priori spectral constraints on the coarse mode spectral coefficients in the visible or the fine mode coefficients in the near IR (where the fine and coarse mode dominate, respectively). The extraction of modal spectral coefficients at different wavelengths can be viewed as an end in itself but can as well lead to simplified inversion procedures for estimating averaged microphysical parameters such as the effective radius of the two modes.

A combination of the bimodal spectral coefficient relations and formal particle size inversion procedures can lead to a simplified "basis set" of spectral coefficient relations which characterizes the optically important climatological features of a given region. Thus the  $\alpha$  versus  $\tau_a$  or  $\alpha'$  versus  $\tau_a$  statistics of a network station can be represented by simple generating equations which can be used, for example, as indicators of aerosol bimodal type for use in radiative transfer models.

The relevance of this analytical approach in the face of sophisticated ground-based inversion techniques requires some comment. Formal inversions for particle size and refractive index are an inevitable and necessary tool for understanding local aerosol dynamics. On the other hand, the bimodal

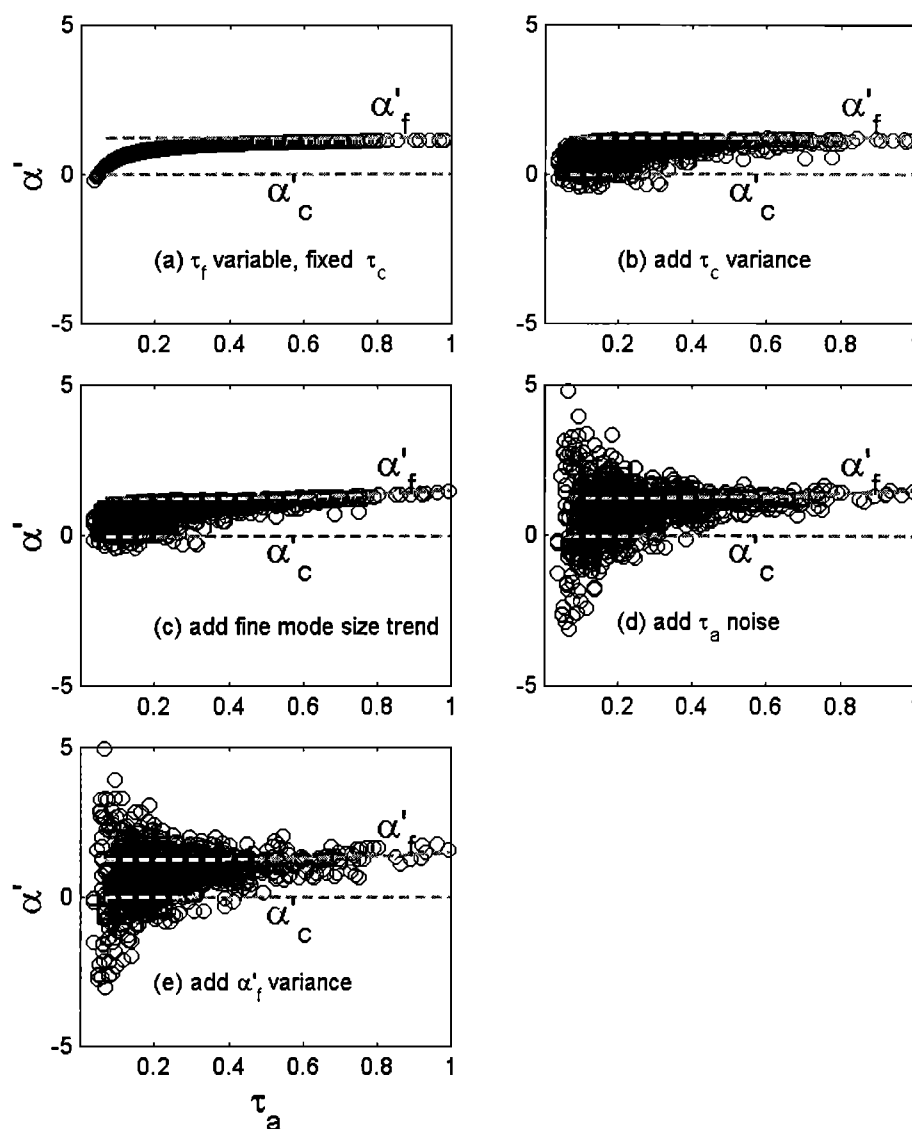


**Figure 11.** Plots of  $\alpha'$  versus  $\tau_a$  at 450 nm wavelength showing sequential simulation steps. The final graph, Figure 11(e), corresponds to the 450 nm simulation in the second row and second column of Figure 9. Details of the simulation steps are given in Table 4.

approach provides a robust basis for comparison with the inversion results and underscores the observation of significant features in the retrieved particle size spectra. Because it is a purely optical approach, it is independent of any smoothing constraints or intermediate parameters employed in the inversions. It is also worth noting that complete inversions which use both spectral and angular information are acquired much less frequently by instruments such as the CIMEL radiometer of AERONET and thus that the type of spectral interpretations presented above apply to a simpler but more temporally continuous data set of optical depth spectra.

In more general terms it is often more appropriate to limit the data interpretation to the extraction of pure optical parameters if the ultimate application is atmospheric radiative transfer. In many circumstances it is arguably advantageous and more efficient to avoid the intermediate microphysical domain by

extracting those key optical parameters which are needed to adequately understand the radiative transfer physics.

The characterization of optical depth spectra in terms of bimodal spectral coefficients is coherent, for example, with the optical inversion strategies developed for the recently launched MODIS sensor. The MODIS inversion algorithms incorporate a radiative transfer approach based on the division of aerosols into fine and coarse modes [Tanré *et al.*, 1997] and, in fact, are focused specifically on inverting  $\eta$ -weighted means of individual modal radiances to estimate  $\tau_a$ ,  $r_{eff}$ , and  $\eta$ . These products can directly be compared with or have a direct link with the spectral parameters presented in this paper and indeed could be recast into the bimodal formulation in order (for example) to characterize the extensive versus intensive contributions to  $\alpha$  within an image.

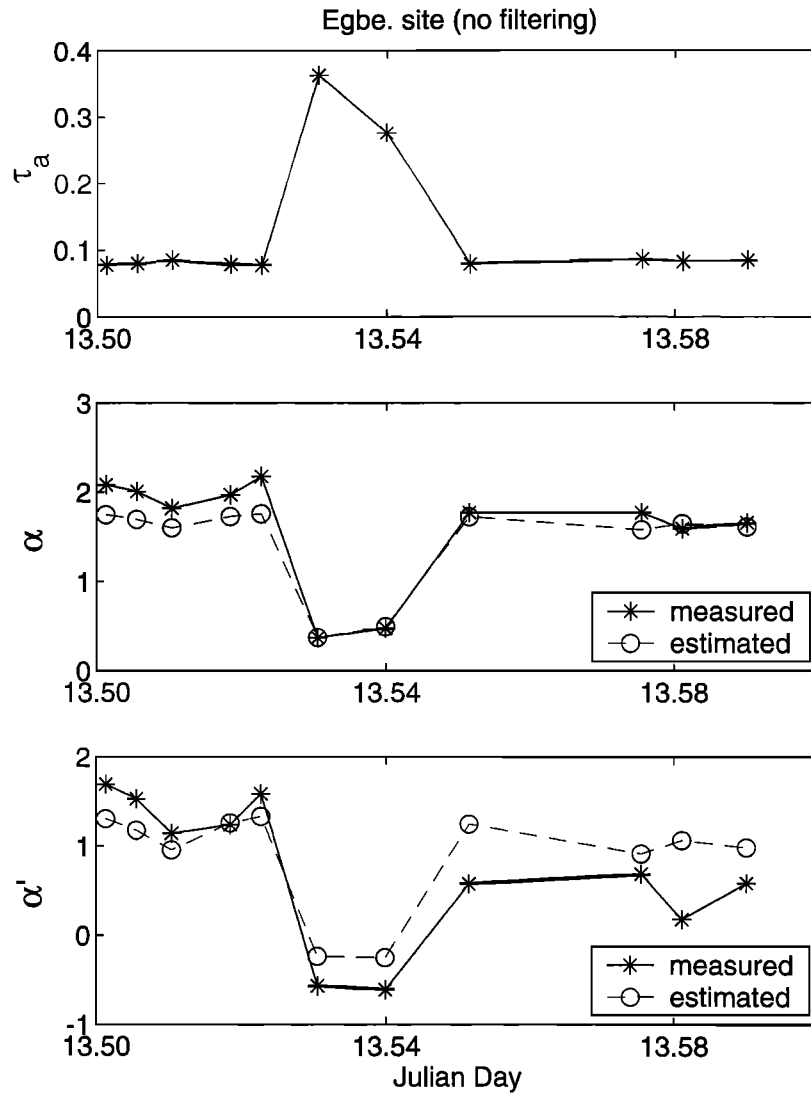


**Figure 12.** Measured and estimated  $\alpha$  and  $\alpha'$  at 500 nm as a function of time for a diurnal thin cloud event. The estimated values were obtained from fixed spectral derivatives for each mode and a time-independent value of  $\tau_f$  (see text for details). These non-cloud-screened data were acquired on August 13, 1998, at Egbert Ontario, Canada, using a CIMEL Sun photometer belonging to the AEROCAN network.

#### Notation

|             |  |           |   |
|-------------|--|-----------|---|
| $A$         | abundance or integrated vertical number density (typical units of particles/cm <sup>2</sup> ). | $C_c$     | coarse mode scattering cross section (typical units of cm <sup>2</sup> ).   |
| $A_f$       | abundance or vertically integrated number density for the fine particle mode.                  | $C_f$     | fine mode scattering cross section (typical units of cm <sup>2</sup> ).   |
| $A_c$       | abundance or vertically integrated number density for the coarse particle mode.                | $\eta$    | optical mixing ratio $\tau_f/\tau_a$ .  |
| $\alpha_c$  | $-d\ln\tau_c/d\ln\lambda$ .  | NIR       | near infrared (taken as 0.35 to 1.05 $\mu\text{m}$ in this paper, a range that roughly corresponds to the CIMEL Sun photometer range).                  |
| $\alpha_f$  | $-d\ln\tau_f/d\ln\lambda$ .  | $r$       | aerosol particle radius (units of $\mu\text{m}$ ).  |
| $\alpha$    | $-d\ln\tau_a/d\ln\lambda$ .  | $r_N$     | modal radius of a lognormal particle size distribution ( $r_N = r_g$ in Hansen and Travis, [1974]).   |
| $\alpha'_f$ | $d\alpha_c/d\ln\lambda$ .  | $r_{eff}$ | optically effective radius of a size distribution as per Hansen and Travis, [1974] ( $= r_N \exp(2.5 \ln^2 \sigma)$ for a lognormal size distribution). |
| $\alpha'_c$ | $d\alpha_f/d\ln\lambda$ .  | $\sigma$  | $\ln \sigma$ is the standard deviation of a log normal size distribution ( $\ln \sigma$ is equal to the $\sigma_g$ used in Hansen and Travis, [1974]).  |
| $\alpha'$   | $d\alpha/d\ln\lambda$ .  |           |   |

|                  |   |
|------------------|---|
| $\sigma(\tau_a)$ | standard deviation of a random, normal distribution of $\tau_a$ values. |
| SWIR             | short wave infrared (roughly 1.0 to 3.5 $\mu\text{m}$ ).                |
| $\tau_c$         | coarse mode optical depth.  |
| $\tau_f$         | fine mode optical depth.  |
| $\tau_a$         | total aerosol optical depth.  |

**Acknowledgments.** The authors thank NASA and the National Science Foundation (NRC) for their generous support. The comments of one of the reviewers were very helpful in revising and clarifying the text and are gratefully acknowledged.

## References

- Ahern, F. J., R. P. Gauthier, P. M. Teillet, J. Sirois, G. Fedosejevs, and D. Lorente, Investigation of continental aerosols with high-spectral-resolution solar extinction measurements, *Appl. Opt.*, **30**(36), 5276-5287, 1991.
- Ångström, A., On the atmospheric transmission of sun radiation and on dust in the air, *Geogr. Ann.*, **11**, 156-166, 1929.
- Dubovik O., and M. D. King, A flexible inversion algorithm for retrieval of aerosol optical properties from Sun and sky radiance measurements, *J. Geophys. Res.*, **105**, 20673-20696, 2000.
- Eck, T. F., B. N. Holben, J. S. Reid, O. Dubovik, A. Smirnov, N. T. O'Neill, I. Slutsker, and S. Kinne, The wavelength dependence of the optical depth of biomass burning, urban and desert dust aerosols, *J. Geophys. Res.*, **104**, 31,333-31,350, 1999.
- Foitzik, L., The spectral extinction of the atmospheric aerosol by Mie particles with different Gaussian distributions, *Beitr. Geophys.*, **74**(3), 199-206, 1964.
- Hansen, J. E., and L. D. Travis, Light scattering in planetary atmospheres, *Space Sci. Rev.*, **16**, 527-610, 1974.
- Holben, B. N., et al., AERONET — A Federated Instrument Network and data archive for aerosol characterization, *Remote Sens. Environ.*, **66**, 1 - 16, 1998.
- Kaufman, Y. J., Aerosol optical thickness and atmospheric path radiance, *J. Geophys. Res.*, **98**, 2677-2692, 1993.
- King, M. D., and D. M. Byrne, A method for inferring total ozone content from the spectral variation of total optical depth obtained with a solar radiometer, *J. Atmos. Sci.*, **33**, 2242-2251, 1976.
- Nikitinskaya, O. D., Barteneva, O. D., and L. K. Veselova, Variations of the atmosphere's spectral (optical) aerosol thickness under conditions of high transparency, *Izv. Atmos. Oceanic Phys.*, **9**(4), 437-442, 1973.
- O'Neill, N. T., and A. Royer, Extraction of bimodal aerosol size distribution radii from spectral and angular slope (Ångström coefficients), *Appl. Opt.*, **32**(9), 1642-1645, 1993.
- Remer, E., Kaufman, Y. J., and B. N. Holben, Interannual variation of ambient aerosol characteristics on the east coast of the United States, *J. Geophys. Res.*, **104**(D2), 2223-2231, 1999.
- Shiffrin, K. S., Simple relationships for the Ångström parameter of disperse systems, *Appl. Opt.*, **34**(21), 4480-4485, 1995.
- Smirnov A., A. Royer, N. T. O'Neill, and A. Tarussov, A study of the link between synoptic air mass type and atmospheric optical parameters, *J. Geophys. Res.*, **99**(D10), 20967-20982, 1994.
- Smirnov A., B.N.Holben, T.F.Eck, O.Dubovik, and I.Slutsker, Cloud screening and quality control algorithms for the AERONET data base, *Rem. Sens. Environ.*, **73**, 337-349, 2000.
- Stettler, M., and W. von Hoyningen-Huene, Estimation of Pinatuba aerosol distribution and its influence on spectral optical thickness measurements in Canada, *Beitr. Geophys.*, **66**(4), 347-354, 1993.
- Tanré, D., L. A. Remer, Y. J. Kaufman, S. Mattoo, P. V. Hobbs, J. M. Livingstone, P. B. Russel, and A. Smirnov, Retrieval of aerosol optical thickness and size distribution over ocean from the MODIS airborne simulator during TARFOX, *J. Geophys. Res.*, **104**, (D2), 2261-2278, 1999.
- Tanré, D., Y. J. Kaufman, M. Herman, and S. Mattoo, Remote sensing of aerosol properties over oceans using the MODIS/EOS spectral radiances, *J. Geophys. Res.*, **102**(D14), 16971-16988, 1997.
- Tomasi, C., E. Caroli, and V. Vitale, Study of the relationship between Ångström's wavelength exponent and Junge particle size distribution exponent, *J. of Clim. Appl. Meteorol.*, **22**, 1707-1716, 1983.
- Villevalde, Yu.V., A. Smirnov, N. T. O'Neill, S. P. Smyshlyayev, and V. V. Yakovlev, Measurement of aerosol optical depth in the Pacific Ocean and the North Atlantic, *J. Geophys. Res.*, **99**(D10), 20983-20988, 1994.
- N. T. O'Neill and A. Royer, CARTEL, Université de Sherbrooke, Sherbrooke, Quebec, Canada, J1K-2R1.
- T. F. Eck, B. N. Holben, A. Smirnov and O. Dubovik, NASA Goddard Space Flight Center, Code 923, Greenbelt, Maryland, 20771.

(Received January 7, 2000; revised April 5, 2000; accepted April 19, 2000.)